Comput Mech (2013) 52:1395–1415
DOI 10.1007/s00466-013-0883-2

ORIGINAL PAPER

Subdomain-based error techniques for generalized finite element approximations of problems with singular stress fields

Felício B. Barros · Clovis S. de Barcellos · C. Armando Duarte · Diego A. F. Torres

Received: 10 September 2012 / Accepted: 17 May 2013 / Published online: 7 June 2013

Abstract This paper considers four types of error measures, each tailored to the generalized finite element method. Particular attention is given to two-dimensional elasticity problems with singular stress fields. The first error measure is obtained using the equilibrated element residual method. The other three estimators overcome the necessity of equilibrating the residue by employing a subdomain strategy. In this strategy, the partition of unity (PoU) property is used to decompose the error problem into local contributions over each patch of elements. The residual functional of the error problem is the same for the subdomain estimators, but the bi-linear form is different for each one of them. In the second estimator, the bi-linear form is weighted by the PoU functions associated with the patch over which the error problem is stated. No weighting appears in the bi-linear form of the third estimator. The fourth measure is proposed as an alternative strategy, in which the products of the PoU functions and test functions are introduced as weights in the weighted integral statement of the differential equation describing the error problem. The linear form of the local error problem is then identical to that of the other subdomain techniques, while the bi-linear form is stated differently, with the PoU functions directly multiplying the test functions. The goal of this study is to investigate the performance of the four estimators in two-dimensional elasticity problems with geometries that produce singularities in the stress field and concentration of the error in the numerical solution.

Keywords Error estimator · Generalized finite element method · Extended finite element method · Two-dimensional singular elasticity singular fields · Subdomain-based residual error estimators

F. B. Barros (✉)
Department of Structural Engineering, Federal University of Minas Gerais, Av. Antônio Carlos 6627, Pampulha, 31270-901 Belo Horizonte, MG, Brazil
e-mail: feliciobbarros@gmail.com; felicio@dees.ufmg.br

C. S. de Barcellos · D. A. F. Torres
Graduate Program in Mechanical Engineering, Federal University of Santa Catarina, 88040-900 Florianópolis, SC, Brazil
e-mail: clovis@grante.ufsc.br

D. A. F. Torres
e-mail: diego.amadeu@gmail.com

C. A. Duarte
2122 Newmark Civil Engineering Laboratory, University of Illinois at Urbana-Champaign, 205, North Mathews Ave., Urbana, IL 61801-2352, USA
e-mail: caduarte@uiuc.edu

1 Introduction

The generalized finite element method (GFEM) can be considered as a special case of the partition of unity method (PUM) [2,4,19,46]. The approximation functions are constructed by extrinsically enriching the partition of unity (PoU) [36], which is generally provided by Lagrangian finite element shape functions. As a result, the approximation functions become associated with nodal points, as in the majority of the so-called meshfree methods. The supports of the PoU functions are patches of elements that share a common node. Such patches are referred to as clouds in the nomenclature of the *hp*-Cloud method [17]. The extrinsic enrichment strategy is similar to that used in the extended finite element method (XFEM) introduced by [9,33]. In these studies, the XFEM was applied to fracture mechanics problems. The method was initially developed using analytical functions to describe discontinuous fields that enrich the PoU near a crack. Despite their independent development, the GFEM and XFEM are closely related and employ the same enrichment approach,

based on the PoU. The two methods are in fact identical according to [10].

The characteristics of the nodal enrichment in the GFEM/-XFEM and other meshfree methods suggest a node-based adaptive scheme to improve the quality of the approximate solution. A good error estimation strategy is essential to accomplish this goal. One of the first studies to address this problem in the context of the GFEM was [47], where a recovery-based error measure is used for h-adapted meshes. The main idea is to find an error measure based on the difference between the computed and improved recovered gradients of the approximation, as it was introduced by [53] for the finite element method (FEM). For the GFEM, an enhanced gradient field can be described using, for example, a basis enriched with handbook functions. This strategy is assessed in [48] using a patch-based indicator; it is shown that the method can yield inaccurate effectivity indices for large relative errors. As noted by [21], the recovery-based error estimation procedure has been employed in the majority of previous studies on the XFEM. Several strategies for obtaining the recovered gradients of the solution field in the XFEM can be found in [11,12,20,23,42,44,52], along with their corresponding error measures. Good performance has been achieved using these strategies in problems with enrichment functions for discontinuities and high gradients.

The first investigation on implicit residual-based error strategies in the GFEM approach was [7]. An error measure was presented along with an adaptive procedure that was specially tailored for the GFEM, based on the element residual method (ERM) [1,37]. In this procedure, an error indicator associated with a patch of elements is calculated from a weighted average of the error indicator of each element belonging to the patch. The improvement in the solution is governed by these patch error indicators and achieved by performing nodal polynomial enrichment. This procedure is explored in [6] for two-dimensional problems, where the non-linear response is modeled using continuum damage mechanics. This method makes it possible to improve the accuracy without excessively increasing the computational cost. However, two drawbacks can be identified. First, the data composing the residual functionals must be equilibrated. Several techniques are available for this equilibration, and in [7], the strategy of [27] is adapted to the GFEM case. The cost of solving the equilibration problem cannot be avoided in the computation of element residual-based error indicators. The problem of equilibrating the residual data is simplified (though not eliminated) in [8] by using a PoU with high continuity. However, the requirement of a large number of quadrature points in the integration of the PoU leads to additional computational cost. The second drawback is that the indicators proposed for the GFEM in [7] are not a natural choice as they are obtained through post-processing of indicators originally evaluated for each element. Despite the good performance, this technique requires improvement, so that an indicator can be directly associated with each patch of elements. [48] propose such an improvement for the GFEM, following the ideas presented in [30,43]. In these papers, the error indicator for the FEM is obtained by solving local problems defined over subdomains, which can be defined as patches of elements, after introducing the PoU concept. In [48], this strategy is extensively evaluated for the GFEM, using a Neumman problem for the Laplacian in a square domain with voids for illustrative purposes. The strategy can change depending on how the PoU function is incorporated into the formulation of the error problem. In the present paper, the behavior of the strategies proposed in [30,43,48] is investigated for the first time in a GFEM analysis of two-dimensional elasticity problems. Polygonal domains presenting smooth and non-smooth solutions are considered. The use of polynomial and non-polynomial enrichment strategies to approximate the solution of the boundary value problem (BVP) is assessed. The error is projected onto a space constructed from polynomial functions one degree higher than that of the approximate solution. A variation on this approach is also considered, in which the residual problem is weighted by the product of the PoU functions and the test functions in the weighted residual method. As a result, the linear form of the local error problem is identical to the standard subdomain technique. However, the bi-linear form is stated in a different way, with the PoU functions directly multiplying the test functions. The consequences of these modifications are discussed and evaluated in several numerical examples.

The goal of this paper is to evaluate the performance of these estimators in two-dimensional elasticity problems with geometries that produce singularities in the stress field and concentration of the error in the numerical solution. Problems of this type have been investigated extensively in the XFEM context but with recovery-based errors, as discussed previously. [42] extend the technique proposed by [53] to represent the enhanced stress field near crack tips in generally inelastic materials. [45] compare the performance of explicit and implicit residual error estimators applied to singular problems in fracture mechanics. The error measures are based on the energy norm and the quantity of interest in a goal-oriented approach but are calculated directly from the element contributions. The explicit residual error estimator is also investigated by [22] for XFEM, where a stable upper bound, measured in the energy norm, is derived and two variants of local error indicators, obtained from different interelement boundary data treatment, are presented.

The remainder of the paper is organized as follows. In Sects. 2 and 3, the GFEM is summarized. The ERM for GFEM approach is reviewed in Sect. 4.1. The subdomain strategy to evaluate the error indicator associated with each patch of elements is described in Sect. 4.2. In the final two

sections, numerical examples are presented, and some final considerations are discussed.

2 The GFEM

As a special case of the PUM, the GFEM has its origins in the following works:

- Babuška and co-workers, initially known as the special FEM [4] and later referred to as the partition of unity FEM [31,32];
- Duarte and Oden, referred to as a meshless formulation of the *hp*-cloud method [16,18] and later as a hybrid approach with the FEM [38].

The basic idea of the GFEM consists of employing a set of PoU functions to enforce interelement continuity. This strategy creates conforming approximations that are improved using an extrinsic nodal enrichment strategy [17]. To summarize the procedure, let us consider, e.g., a conventional linear finite element mesh, $\{\mathcal{K}_E\}_{e=1}^{NE}$ (where NE is the number of elements $\mathcal{K}_E$), defined by N nodes,$\{\boldsymbol{x}_j\}_{j=1}^{N}$, in a domain Ω (see Fig. 1a). A generic patch of elements $\omega_j \in \Omega$ is obtained from the union of the finite elements sharing the vertex node $\boldsymbol{x}_j$. The aggregation of the Lagrangian interpolating functions belonging to each element and associated with node $\boldsymbol{x}_j$ composes the function $\mathcal{N}_j(\boldsymbol{x})$ defined over the support (patch of elements) ω_j. Since $\sum_{j=1}^{N}\mathcal{N}_j(\boldsymbol{x}) = 1$ at every point $\boldsymbol{x}$ in the domain Ω, the set of functions $\{\mathcal{N}_j(\boldsymbol{x})\}_{j=1}^{N}$ constitutes a PoU.

First, a set of n_j linearly independent functions must be defined for each patch ω_j, as follows:

$$\mathcal{I}_j = \left\{L_{jk}^{p}(\bar{\boldsymbol{x}})\right\}_{k=1}^{n_j^p} \cup \left\{L_{jl}^{s}(x)\right\}_{l=1}^{n_j^s} \tag{1}$$

where $\left\{L_{jk}^{p}(\bar{\boldsymbol{x}})\right\}_{k=1}^{n_j^p}$ represents a set of n_j^p polynomial functions, in which the unit polynomial is included ($L_{j1}^{p}(\bar{\boldsymbol{x}}) = 1$), $\left\{L_{jl}^{s}(\boldsymbol{x})\right\}_{l=1}^{n_j^s}$ is a set of n_j^s non-polyonomial special functions used to describe the singularity of the stress field when present, and $n_j^p + n_j^s = n_j$. The superscript p refers to the degree of the complete polynomial space spanned by the GFEM approximation functions after performing the following enrichment strategy. The polynomials $\left\{L_{jk}^{p}(\bar{\boldsymbol{x}})\right\}_{k=1}^{n_j^p}$ are described in terms of non-dimensional coordinate $\bar{\boldsymbol{x}} = \frac{\boldsymbol{x}-\boldsymbol{x}_j}{h_j}$ for each patch ω_j, where h_j is a characteristic size of ω_j, [19]. Note that this transformation is linear, continuous and robust to element distortions.

The generalized finite element approximation functions are determined by the enrichment of the PoU functions. This enrichment is obtained by multiplying such functions by each of the components of (1) for the generic patch ω_j:

$$\{\phi_{ji}\}_{i=1}^{n_j} = \mathcal{N}_j(\boldsymbol{x}) \times \left\{\left\{L_{jk}^{p}(\bar{\boldsymbol{x}})\right\}_{k=1}^{n_j^p} \cup \left\{L_{jl}^{s}(\boldsymbol{x})\right\}_{l=1}^{n_j^s}\right\} \tag{2}$$

with no summation over j.

Figure 1 illustrates the construction of a generalized finite element shape function in $\Re^2$, for the specific case of the bilinear Lagrangean PoU functions. The enrichment scheme is obtained by multiplying a PoU function of C^0-continuity and with compact support ω_j (Fig. 1b) by the enrichment polynomial function $L_{jk}^{p}(\bar{\boldsymbol{x}})$ (Fig. 1c) provided in [46]. The resulting approximation function $\phi_{jk}(\boldsymbol{x})$ (Fig. 1d) inherits characteristics of both functions, e.g., the compact support and continuity of the PoU and the approximate character of the enrichment function.

The generalized global approximation for a function, denoted by $\tilde{\boldsymbol{u}}(\boldsymbol{x})$, can be described as a linear combination of the approximation functions (2) associated with each node $\boldsymbol{x}_j$:

$$\tilde{\boldsymbol{u}}(\boldsymbol{x}) = \sum_{j=1}^{N}\mathcal{N}_j(\boldsymbol{x})\left\{\boldsymbol{u}_j + \sum_{k=2}^{n_j^p} L_{jk}^{p}(\bar{\boldsymbol{x}})\boldsymbol{b}_{jk}^{p} + \sum_{l=1}^{n_j^s} L_{jl}^{s}(\boldsymbol{x})\boldsymbol{b}_{jl}^{s}\right\} \tag{3}$$

where $\boldsymbol{u}_j$, b_{jk}^{p} and b_{jl}^{s} are nodal parameters associated with the approximation functions $\mathcal{N}_j(\boldsymbol{x})$, $\mathcal{N}_j(\boldsymbol{x})L_{jk}^{p}(\bar{\boldsymbol{x}})$ and $\mathcal{N}_j(\boldsymbol{x})L_{jl}^{s}(\boldsymbol{x})$, respectively. The continuity of $\tilde{\boldsymbol{u}}(\boldsymbol{x})$ is guaranteed by the compact support of the PoU ($\mathcal{N}_j(\boldsymbol{x}) = 0$ on the boundary of ω_j), which also allows the combination of different enrichment functions ($L_{jk}^{p}(\bar{\boldsymbol{x}})$ and $L_{jl}^{s}(\boldsymbol{x})$) specifically chosen for each patch ω_j.

3 The model BVP—fundamental equations

In this section, the GFEM is used to solve the following two-dimensional linear elasticity BVP:

$$\text{Find } \boldsymbol{u} \text{ such that } \begin{cases} \nabla\cdot\boldsymbol{\sigma}(\boldsymbol{u}) + \boldsymbol{b} = \boldsymbol{0} & \text{in} \quad \Omega \\ \boldsymbol{u} = \hat{\boldsymbol{u}} & \text{on} \quad \Gamma_D \\ \boldsymbol{t}(\boldsymbol{u}) = \hat{\boldsymbol{t}} & \text{on} \quad \Gamma_N \end{cases} \tag{4}$$

where $\Omega \in \mathbb{R}^2$ is the domain problem, $\boldsymbol{u}^T \overset{\text{def}}{=} [u_x \; u_y]$ is a vector representing the displacement field, Γ_D and Γ_N denote complementary parts of the boundary $\partial\Omega$ where the Dirichlet and Neumann conditions hold, respectively, $\boldsymbol{\sigma} = \boldsymbol{D}\boldsymbol{\varepsilon}$ is the stress tensor, $\boldsymbol{\varepsilon}$ is the strain tensor, $\boldsymbol{D}$ is the constitutive rigidity tensor, $\boldsymbol{b}$ is the vector of body forces, $\boldsymbol{t} = \boldsymbol{\sigma}\cdot\boldsymbol{n}$ is

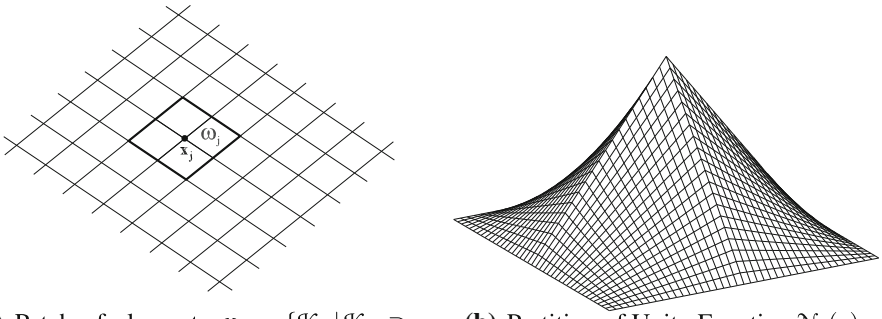

Fig. 1 Enrichment scheme for a patch ω_j, adopted from [8]

(a) Patch of elements $\omega_j = \{\mathcal{K}_E | \mathcal{K}_E \supset x_j\}$

(b) Partition of Unity Function $\mathcal{N}_j(x)$

(c) Enrichment Function $L^p_{jk}(\bar{x})$

(d) Enriched Approximation Function $\phi_{jk} = \mathcal{N}_j(x) L^p_{jk}(\bar{x})$, no summation over j

the traction vector, $\hat{\boldsymbol{u}}$ and $\hat{\boldsymbol{t}}$ are prescribed displacement and traction vectors, $\boldsymbol{n}$ is the unit normal on the boundary $\partial\Omega$.

The corresponding variational form of this problem can be stated as follows:

Find $\boldsymbol{u} \in \mathcal{U}$, such that

$$\mathcal{B}(\boldsymbol{u}, \boldsymbol{v}) = \mathcal{F}(\boldsymbol{v}) \;\forall\; \boldsymbol{v} \in \mathcal{V} \tag{5}$$

where $\mathcal{U}$ and $\mathcal{V} \subset \mathcal{H}^1(\Omega)$, are the set of kinematically admissible functions and the space of admissible variations, respectively, $\mathcal{H}^1(\Omega)$ is the Hilbert space of order 1, the following variational operators are defined:

$$\mathcal{B}(\boldsymbol{u}, \boldsymbol{v}) = \iint_{\Omega} \boldsymbol{\varepsilon}^T(\boldsymbol{v}) \boldsymbol{\sigma}(\boldsymbol{u})\, d\Omega$$

$$\mathcal{F}(\boldsymbol{v}) = \iint_{\Omega} \boldsymbol{v}^T \boldsymbol{b}\, d\Omega + \int_{\Gamma_N} \boldsymbol{v}^T \hat{\boldsymbol{t}}\, d\Gamma$$

$\boldsymbol{v}^T \overset{\text{def}}{=} [v_x\, v_y]$ is the transposed test function vector, $\boldsymbol{\varepsilon}(\boldsymbol{v})$ is obtained from the symmetric part of the gradient of $\boldsymbol{v}$.

Now let $\tilde{\mathcal{U}} \subset \mathcal{U}$ be the subset spanned by a set of kinematically admissible GFEM functions constructed as in (2), and let $\tilde{\mathcal{V}}$ be the corresponding subspace of $\mathcal{V}$. The Galerkin approximation of (5) then proceeds as follows.

Find $\tilde{\boldsymbol{u}} \in \tilde{\mathcal{U}}$, such that:

$$\mathcal{B}(\tilde{\boldsymbol{u}}, \tilde{\boldsymbol{v}}) = \mathcal{F}(\tilde{\boldsymbol{v}}) \;\forall\; \tilde{\boldsymbol{v}} \in \tilde{\mathcal{V}} \tag{6}$$

where $\tilde{\boldsymbol{u}}$ and $\tilde{\boldsymbol{v}}$ are obtained from Expression (3) as follows:

$$\tilde{\boldsymbol{u}}(\boldsymbol{x}) = \sum_{j=1}^{N} \mathcal{N}_j(\boldsymbol{x}) \left\{ \boldsymbol{u}_j + \sum_{k=2}^{n_j^p} L^p_{jk}(\bar{\boldsymbol{x}}) \boldsymbol{b}^p_{jk} + \sum_{l=1}^{n_j^s} L^s_{jl}(\boldsymbol{x}) \boldsymbol{b}^s_{jl} \right\} \tag{7}$$

$$\tilde{\boldsymbol{v}}(\boldsymbol{x}) = \sum_{j=1}^{N} \mathcal{N}_j(\boldsymbol{x}) \left\{ \boldsymbol{v}_j + \sum_{k=2}^{n_j^p} L^p_{jk}(\bar{\boldsymbol{x}}) \boldsymbol{c}^p_{jk} + \sum_{l=1}^{n_j^s} L^s_{jl}(\boldsymbol{x}) \boldsymbol{c}^s_{jl} \right\} \tag{8}$$

Here, $\boldsymbol{v}_j$, c^p_{jk} and c^s_{jl} are the nodal parameters of the test functions associated with the approximation functions given by $\mathcal{N}_j(\boldsymbol{x})$, $\mathcal{N}_j(\boldsymbol{x}) L^p_{jk}(\bar{\boldsymbol{x}})$ and $\mathcal{N}_j(\boldsymbol{x}) L^s_{jl}(\boldsymbol{x})$, respectively.

Expressions (7) and (8) can be rewritten using the following vectorial representation:

$$\tilde{\boldsymbol{u}}(\boldsymbol{x}) = \boldsymbol{\Phi}^T \cdot \boldsymbol{U} \tag{9}$$

$$\tilde{\boldsymbol{v}}(\boldsymbol{x}) = \boldsymbol{\Phi}^T \cdot \boldsymbol{V} \tag{10}$$

where the vector $\boldsymbol{\Phi}^T = \left[\boldsymbol{\phi}_j^T\right]_{j=1}^{N}$ consists of the following elements associated with each of the N patches ω_j:

$$\boldsymbol{\phi}_j^T = \left[\mathcal{N}_j(\boldsymbol{x}) \quad \left[\mathcal{N}_j(\boldsymbol{x})\, L^p_{jk}(\bar{\boldsymbol{x}})\right]_{k=2}^{n_j^p} \right.$$

$$\left[\mathcal{N}_j(\boldsymbol{x})\, L^s_{jl}(\boldsymbol{x})\right]_{l=1}^{n^s_j}\Bigg] \tag{11}$$

and, analogously, the vectors of parameters $\boldsymbol{U}^T = \left[\boldsymbol{u}_j^T\right]_{j=1}^{N}$ and $\boldsymbol{V}^T = \left[\boldsymbol{v}_j^T\right]_{j=1}^{N}$ consist of the following elements:

$$\boldsymbol{u}_j^T = \left[\boldsymbol{u}_j \quad \left[\boldsymbol{b}^p_{jk}\right]_{k=2}^{n^s_j} \quad \left[\boldsymbol{b}^s_{jl}\right]_{l=1}^{n^p_j}\right]$$
$$\boldsymbol{v}_j^T = \left[\boldsymbol{v}_j \quad \left[\boldsymbol{c}^p_{jk}\right]_{k=2}^{n^s_j} \quad \left[\boldsymbol{c}^s_{jl}\right]_{l=1}^{n^p_j}\right]$$

4 Error estimator

In [7], a p-adaptive procedure is tailored to the nodal enrichment approach of the GFEM. The ERM introduced in [5,14] is used to estimate the energy norm of the local approximation of the error. The local measure is the error indicator and can be evaluated at the element level by solving a local BVP defined over each element. For each element, the data comprising the local error problem are equilibrated using the strategy proposed by [27]. To obtain a measure that can be used in an adaptive strategy for the GFEM, it is necessary to define another error indicator associated with each patch. This indicator is obtained by considering a measure such as the average value of the error indicators of the elements that share each vertex node, weighted, for instance, by their volume. This is certainly not a natural choice, but a post-processing approach to the error problem, which can deteriorate the nodal indicators even when the element measures provide good approximations of the energy norm of the local error. A more suitable strategy is proposed for the GFEM by [48], in the form of an extension of the subdomain error estimator proposed by [43,30,39] for FEM. In this strategy, the problem is defined over patches of elements, so that the resulting indicators are directly related to the nodes associated with the patches rather than with the elements. In the next two sections, these two approaches to error measures (based on elements or subdomains) are summarized. First, a global equation that represents the error problem is presented.

Let $\boldsymbol{u} \in \mathcal{U}$ be the true solution of the BVP (5), and let $\tilde{\boldsymbol{u}} \in \tilde{\mathcal{U}}$ be the approximate solution of problem (6). The error of the approximate solution $\boldsymbol{e} \in \mathcal{U}$ can be defined as:

$$\boldsymbol{e} \overset{\text{def}}{=} \boldsymbol{u} - \tilde{\boldsymbol{u}} \tag{12}$$

Considering the linearity of the bi-linear functional $\mathcal{B}(\cdot,\cdot)$, it can be shown that:

$$\mathcal{B}(\boldsymbol{u}, \boldsymbol{v}) = \mathcal{B}(\boldsymbol{e} + \tilde{\boldsymbol{u}}, \boldsymbol{v}) = \mathcal{F}(\boldsymbol{v}) \tag{13}$$
$$\mathcal{B}(\boldsymbol{e}, \boldsymbol{v}) = \mathcal{F}(\boldsymbol{v}) - \mathcal{B}(\tilde{\boldsymbol{u}}, \boldsymbol{v}) \tag{14}$$

A global variational equation for the error can be recovered as follows.

Find $\boldsymbol{e} \in \mathcal{U}$, such that

$$\mathcal{B}(\boldsymbol{e}, \boldsymbol{v}) = \mathcal{R}(\boldsymbol{v}) \;\forall\; \boldsymbol{v} \in \mathcal{V} \tag{15}$$

where the residual functional is defined as

$$\mathcal{R}(\boldsymbol{v}) = \mathcal{F}(\boldsymbol{v}) - \mathcal{B}(\tilde{\boldsymbol{u}}, \boldsymbol{v}) \tag{16}$$

Here, it is assumed without loss of generality that the essential boundary conditions are exactly satisfied.

To reduce the computational cost of solving (15) and compute a local indicator for adaptive purposes, the global problem can be replaced by a set of local problems. New boundary conditions must be imposed to ensure the solvability of the problems and quality of the error estimation.

4.1 Implicit ERM

In the implicit ERM, problem (15) is decomposed into a set of local problems defined over each element $\mathcal{K}_E$, as follows.

Find $\boldsymbol{e}^{\mathcal{K}_E} \in \mathcal{U}(\mathcal{K}_E)$, such that

$$\mathcal{B}_{\mathcal{K}_E}(\boldsymbol{e}^{\mathcal{K}_E}, \boldsymbol{v}) = \mathcal{R}_{\mathcal{K}_E}(\boldsymbol{v}) \;\;\forall\;\; \boldsymbol{v} \in \mathcal{V}(\mathcal{K}_E) \tag{17}$$

where $\mathcal{U}(\mathcal{K}_E)$ and $\mathcal{V}(\mathcal{K}_E)$ are spaces of restrictions from $\mathcal{U}$ and $\mathcal{V}$ on $\mathcal{K}_E$ respectively and the residual functional is defined as

$$\mathcal{R}_{\mathcal{K}_E}(\boldsymbol{v}) = \mathcal{F}_{\mathcal{K}_E}(\boldsymbol{v}) - \mathcal{B}_{\mathcal{K}_E}(\tilde{\boldsymbol{u}}, \boldsymbol{v}) \tag{18}$$

with

$$\mathcal{B}_{\mathcal{K}_E}(\boldsymbol{e}^{\mathcal{K}_E}, \boldsymbol{v}) = \iint_{\mathcal{K}_E} \boldsymbol{\varepsilon}^T(\boldsymbol{v})\boldsymbol{\sigma}(\boldsymbol{e})\, d\Omega \tag{19}$$

$$\mathcal{F}_{\mathcal{K}_E}(\boldsymbol{v}) = \iint_{\mathcal{K}_E} (\boldsymbol{v})^T \boldsymbol{b}\, d\Omega + \int_{\partial\mathcal{K}_E \cap \Gamma_N} (\boldsymbol{v})^T \hat{\boldsymbol{t}}\, d\Gamma + \int_{\partial\mathcal{K}_E \setminus \partial\Omega} (\boldsymbol{v})^T \left[\boldsymbol{t} - \boldsymbol{t}(\tilde{\boldsymbol{u}})\right] d\Gamma \tag{20}$$

$$\mathcal{B}_{\mathcal{K}_E}(\tilde{\boldsymbol{u}}, \boldsymbol{v}) = \iint_{\mathcal{K}_E} \boldsymbol{\varepsilon}^T(\boldsymbol{v})\boldsymbol{\sigma}(\tilde{\boldsymbol{u}})\, d\Omega \tag{21}$$

The last term of (20) arises from the decomposition of the global error problem into local ones. The term results from a new boundary condition that must be imposed at the edges between $\mathcal{K}_E$ and its neighboring elements, $(\partial\mathcal{K}_E \setminus \partial\Omega)$. Clearly, the true traction $\boldsymbol{t}$ is unknown; this fact together with the infinite-dimensional character of the solution space $\mathcal{U}(\mathcal{K}_E)$ preclude the computation of the error. To compute an approximation to the error, [37] replaces the exact error $\boldsymbol{e}$ with an approximation, $\tilde{\boldsymbol{e}}$, which lies in a finite dimensional bubble-like function space for the finite elements. In [7], an equivalent space is constructed from the set of polynomial approximation functions used in the GFEM. In this case, the

compact support of each function takes on a "patch-bubble-like" character, following the concept illustrated in Figure 1. Accounting for the previous considerations, the polynomial error space $\mathcal{X}^0_{p+q}(\mathcal{K}_E)$ can be defined in each element as follows:

$$\mathcal{X}^0_{p+q}(\mathcal{K}_E) = \left\{\tilde{\boldsymbol{v}}_{p+q} \in \mathcal{U}_{p+q}(\mathcal{K}_E);\ \Pi_p(\tilde{\boldsymbol{v}}_{p+q}) = 0;\ \tilde{\boldsymbol{v}}_{p+q} = 0 \text{ on } \partial\mathcal{K}_E \cap \Gamma_D\right\} \tag{22}$$

where $\Pi_p : \mathcal{U}_{p+q}(\mathcal{K}_E) \rightarrow \mathcal{U}_p(\mathcal{K}_E)$ is a local interpolation operator defined according to [37]. $\mathcal{U}_p(\mathcal{K}_E)$ and $\mathcal{U}_{p+q}(\mathcal{K}_E)$ denote spaces of polynomial order up to p and $p+q$ respectively. These spaces are spanned by the set of functions (2) for all ω_j covering the element $\mathcal{K}_E$. The set $\left\{L^p_{jk}(\bar{\boldsymbol{x}})\right\}_{k=1}^{n_j^p}$ forms a basis for the polynomial space of order up to p or $p+q$, and the set $\left\{L^s_{jl}(\boldsymbol{x})\right\}_{l=1}^{n_j^s} = 0$. The motivation for this choice is the assumption that the error can be approximated by the polynomial terms with degree q higher than that of the approximate solution space $\tilde{\mathcal{U}} \supset \mathcal{U}_p$. The parameter q can be chosen so that a better approximation to the error can be found. However, when the true solution $\boldsymbol{u}$ is not smooth, it may be not effective to increase q unless the special functions ($L^s_{jl}(\boldsymbol{x})$ in (1)) used to construct $\tilde{\boldsymbol{u}}$ are able to represent the non-smooth behavior of the solution.

A new BVP can now be formulated for each element $\mathcal{K}_E$ of a patch and expressed in the following variational form.

Find $\tilde{\boldsymbol{e}}^{\mathcal{K}_E}_{p+q} \in \mathcal{X}^0_{p+q}(\mathcal{K}_E)$, such that:

$$\mathcal{B}_{\mathcal{K}_E}(\tilde{\boldsymbol{e}}^{\mathcal{K}_E}_{p+q}, \tilde{\boldsymbol{v}}_{p+q}) = \mathcal{R}_{\mathcal{K}_E}(\tilde{\boldsymbol{v}}_{p+q}) \quad \forall\ \tilde{\boldsymbol{v}}_{p+q} \in \mathcal{X}^0_{p+q}(\mathcal{K}_E) \tag{23}$$

where the residual functional is defined as

$$\mathcal{R}_{\mathcal{K}_E}(\tilde{\boldsymbol{v}}_{p+q}) = \mathcal{F}^a_{\mathcal{K}_E}(\tilde{\boldsymbol{v}}_{p+q}) - \mathcal{B}_{\mathcal{K}_E}(\tilde{\boldsymbol{u}}, \tilde{\boldsymbol{v}}_{p+q}) \tag{24}$$

and

$$\mathcal{B}_{\mathcal{K}_E}(\tilde{\boldsymbol{e}}^{\mathcal{K}_E}_{p+q}, \tilde{\boldsymbol{v}}_{p+q}) = \iint_{\mathcal{K}_E} \boldsymbol{\varepsilon}^T(\tilde{\boldsymbol{v}}_{p+q})\boldsymbol{\sigma}(\tilde{\boldsymbol{e}}^{\mathcal{K}_E}_{p+q})\, d\Omega \tag{25}$$

$$\begin{aligned}\mathcal{F}^a_{\mathcal{K}_E}(\tilde{\boldsymbol{v}}_{p+q}) = &\iint_{\mathcal{K}_E} (\tilde{\boldsymbol{v}}_{p+q})^T \boldsymbol{b}\, d\Omega \\ &+ \int_{\partial\mathcal{K}_E \cap \Gamma_N} (\tilde{\boldsymbol{v}}_{p+q})^T \hat{\boldsymbol{t}}\, d\Gamma \\ &+ \int_{\partial\mathcal{K}_E \setminus \partial\Omega} (\tilde{\boldsymbol{v}}_{p+q})^T \left[\langle \boldsymbol{t}(\tilde{\boldsymbol{u}})\rangle_a - \boldsymbol{t}(\tilde{\boldsymbol{u}})\right] d\Gamma\end{aligned} \tag{26}$$

$$\mathcal{B}_{\mathcal{K}_E}(\tilde{\boldsymbol{u}}, \tilde{\boldsymbol{v}}_{p+q}) = \iint_{\mathcal{K}_E} \boldsymbol{\varepsilon}^T(\tilde{\boldsymbol{v}}_{p+q})\boldsymbol{\sigma}(\tilde{\boldsymbol{u}})\, d\Omega \tag{27}$$

In the above formulation, $\tilde{\boldsymbol{e}}^{\mathcal{K}_E}_{p+q}$ is the Galerkin approximation of the error function $\boldsymbol{e}$, which defines the error indicator function, and $\tilde{\boldsymbol{v}}_{p+q}$ is the test function of the problem. Both are described by the GFEM functions as follows:

$$\tilde{\boldsymbol{e}}^{\mathcal{K}_E}_{p+q} = (\boldsymbol{\Phi}^{\mathcal{K}_E}_{p+q})^T \boldsymbol{I}^{\mathcal{K}_E} \tag{28}$$

$$\tilde{\boldsymbol{v}}_{p+q} = (\boldsymbol{\Phi}^{\mathcal{K}_E}_{p+q})^T \boldsymbol{V}^{\mathcal{K}_E} \tag{29}$$

where the vector of polynomial approximation functions $\boldsymbol{\Phi}^{\mathcal{K}_E}_{p+q} = \left[(\boldsymbol{\phi}^{\mathcal{K}_E}_{p+q})^T_j\right]_{j=1}^{N_{\mathcal{K}_E}}$ is composed of the following vectors associated with the $N_{\mathcal{K}_E}$ patches ω_j that cover the element $\mathcal{K}_E$:

$$(\boldsymbol{\phi}^{\mathcal{K}_E}_{p+q})^T_j = \left[\mathcal{N}_j(\boldsymbol{x})\, L^p_{jk}(\bar{\boldsymbol{x}})\right]_{k=n_j^p+1}^{n_j^p+n_j^q} \tag{30}$$

and the vectors

$$\left(\boldsymbol{I}^{\mathcal{K}_E}\right)^T = \left[\left(\left[\boldsymbol{i}^{\mathcal{K}_E}_k\right]_{k=n_j^p+1}^{n_j^p+n_j^q}\right)^T_j\right]_{j=1}^{N_{\mathcal{K}_E}}$$

$$\left(\boldsymbol{V}^{\mathcal{K}_E}\right)^T = \left[\left(\left[\boldsymbol{v}^{\mathcal{K}_E}_k\right]_{k=n_j^p+1}^{n_j^p+n_j^q}\right)^T_j\right]_{j=1}^{N_{\mathcal{K}_E}}$$

are nodal parameter vectors associated with each approximation function of (30). The vector $\boldsymbol{I}^{\mathcal{K}_E}$ is called the vector of error indicators. Here, $n_j^p + n_j^q$ is the number of functions $L^p_{jk}(\bar{\boldsymbol{x}})$ necessary to obtain an approximation that can represent a complete polynomial of degree $p+q$.

Note that in the last term of (26), the unknown true traction is replaced by $\langle \boldsymbol{t}(\tilde{\boldsymbol{u}})\rangle_a = 1/2\{\boldsymbol{t}(\tilde{\boldsymbol{u}}) + \boldsymbol{t}(\tilde{\boldsymbol{u}}^*)\}$, which denotes the average of the approximate tractions evaluated on $\partial\mathcal{K}_E \setminus \partial\Omega$ from the values $\boldsymbol{t}(\tilde{\boldsymbol{u}})$ defined for $\mathcal{K}_E$ and its neighboring elements ($\boldsymbol{t}(\tilde{\boldsymbol{u}}^*)$). The superscript a of the operator $\mathcal{F}^a_{\mathcal{K}_E}(\cdot)$ differentiates it from (20), where the true traction is used.

When $\mathcal{K}_E$ is an inner element, the BVP (23) corresponds to a Neumman problem as it involves only natural boundary conditions. The problem being approximated may therefore not have a unique solution. A strategy to solve this problem by equilibrating the boundary data with the interior residuals is presented in [7] for the GFEM, following the method proposed by [27]. This strategy is used in the numerical examples in this paper. A detailed discussion of this strategy is beyond the scope of the present work and can be found in the cited references.

After imposing the equilibrated data, problem (23) can be solved locally. The local values of the energy norm of the functions $\tilde{\boldsymbol{e}}_{p+q}$ obtained for each element can be estimated as follows:

$$\mathcal{E}_1^{\mathcal{K}_E} \overset{\text{def}}{=} ||\tilde{\boldsymbol{e}}^{\mathcal{K}_E}_{p+q}||_{U(\mathcal{K}_E)} = \left[\mathcal{B}_{\mathcal{K}_E}(\tilde{\boldsymbol{e}}^{\mathcal{K}_E}_{p+q}, \tilde{\boldsymbol{e}}^{\mathcal{K}_E}_{p+q})\right]^{1/2} \tag{31}$$

where $\mathcal{E}_1^{\mathcal{K}_E}$ defines the error indicator for the element $\mathcal{K}_E$. The global error estimator is computed from the contribution of the local indicators:

$$\mathcal{E}_1 = ||\tilde{\boldsymbol{e}}^{\mathcal{K}_E}_{p+q}||_U = \sqrt{\sum_{\mathcal{K}_E \in \Omega} (\mathcal{E}_1^{\mathcal{K}_E})^2} \tag{32}$$

A simple way to define the error measure associated with each patch ω_j is using the weighted average of the error indicators, given by (31), of the elements $\mathcal{K}_E$ contained in ω_j. Therefore, a nodal error indicator can be defined as:

$$\mathcal{E}_1^{\omega_j} \stackrel{\text{def}}{=} \sum_{\mathcal{K}_E \in \omega_j} \frac{V_{\mathcal{K}_E} ||\tilde{\boldsymbol{e}}^{\mathcal{K}_E}_{p+q}||_{U(\mathcal{K}_E)}}{V_{\omega_j}} \tag{33}$$

where the volume of each element $V_{\mathcal{K}_E}$ is employed as the weight and $V_{\omega_j} = \sum_{\mathcal{K}_E \in \omega_j} V_{\mathcal{K}_E}$ is the total volume of the patch ω_j. The index 1 is used to differentiate this estimator from those presented in the following sections.

4.2 Implicit subdomain residual method

In [30,39], problem (15) is decomposed into local contributions over a patch of elements, referred to by the authors as stars, for a finite element problem. In the case of the GFEM, this geometric entity shares the same meaning as the patch ω_j in this paper, that is, the support of a partition of unity function $\mathcal{N}_j$ associated with the node $\boldsymbol{x}_j$. [48] follows the same approach for the GFEM, but refers to this entity as a patch or even a subdomain. In the following, such nomenclature refers to the subdomain over which the local error problem is stated.

Let problem (15) be rewritten using the partition of unity concept and the linear property of the residual functional:

$$\mathcal{B}(\boldsymbol{e}, \boldsymbol{v}) = \mathcal{R}(\boldsymbol{v}) = \mathcal{R}\left(\boldsymbol{v} \sum_{j=1}^{N} \mathcal{N}_j\right) = \sum_{j=1}^{N} \mathcal{R}(\mathcal{N}_j \boldsymbol{v}) \tag{34}$$

The linear Lagrangian functions $\mathcal{N}_j$ are adopted here but they could be replaced by any type of partition of unity.

Because $\mathcal{R}(\mathcal{N}_j \boldsymbol{v}) = 0$ when $\omega_j \cap \text{supp}(\boldsymbol{v}) = \emptyset$, the residue can be decomposed into local contributions, defined over each patch. Using (34) and following [43], problem (15) can be replaced by a set of local problems defined over each patch ω_j:

Find $\boldsymbol{e}^{\omega_j} \in \mathcal{U}(\omega_j)$, such that

$$\mathcal{B}^{\zeta_j}_{\omega_j}(\boldsymbol{e}^{\omega_j}, \boldsymbol{v}) = \mathcal{R}_{\omega_j}(\mathcal{N}_j \boldsymbol{v}) \quad \forall\, \boldsymbol{v} \in \mathcal{V}(\omega_j) \tag{35}$$

where $\mathcal{U}(\omega_j)$ and $\mathcal{V}(\omega_j)$ are spaces of restrictions from $\mathcal{U}$ and $\mathcal{V}$ on ω_j, respectively, and the residual functional is defined as

$$\mathcal{R}_{\omega_j}(\mathcal{N}_j \boldsymbol{v}) = \mathcal{F}_{\omega_j}(\mathcal{N}_j \boldsymbol{v}) - \mathcal{B}_{\omega_j}(\tilde{\boldsymbol{u}}, \mathcal{N}_j \boldsymbol{v}) \tag{36}$$

and

$$\mathcal{B}^{\zeta_j}_{\omega_j}(\boldsymbol{e}^{\omega_j}, \boldsymbol{v}) = \iint_{\omega_j} \zeta_j \boldsymbol{\varepsilon}^T(\boldsymbol{v}) \boldsymbol{\sigma}(\boldsymbol{e}^{\omega_j})\, d\Omega \tag{37}$$

$$\mathcal{F}_{\omega_j}(\mathcal{N}_j \boldsymbol{v}) = \iint_{\omega_j} (\mathcal{N}_j \boldsymbol{v})^T \boldsymbol{b}\, d\Omega + \int_{\partial\omega_j \cap \Gamma_N} (\mathcal{N}_j \boldsymbol{v})^T \hat{\boldsymbol{t}}\, d\Gamma \tag{38}$$

$$\mathcal{B}_{\omega_j}(\tilde{\boldsymbol{u}}, \mathcal{N}_j \boldsymbol{v}) = \iint_{\omega_j} \boldsymbol{\varepsilon}^T(\mathcal{N}_j \boldsymbol{v}) \boldsymbol{\sigma}(\tilde{\boldsymbol{u}})\, d\Omega \tag{39}$$

In Expression (37), ζ_j represents a weighting function. If the approach proposed by [43] is adopted, then $\zeta_j = \mathcal{N}_j$, i.e., it is the PoU function associated with the patch ω_j. In contrast, $\zeta_j = 1$ in the strategy employed by [48].

According to [43,48], the following theoretical upper estimator can be defined by summing the local measures associated with each patch:

$$\mathcal{E}_k^U = \sqrt{M} \sqrt{\sum_{j=1}^{N} ||\boldsymbol{e}^{\omega_j}||^2_{U(\omega_j)}} = \sqrt{M} \sqrt{\sum_{j=1}^{N} \mathcal{B}^{\zeta}_{\omega_j}(\boldsymbol{e}^{\omega_j}, \boldsymbol{e}^{\omega_j})} \tag{40}$$

where the index k indicates the estimators associated with the choice for ζ_j in Expression (37):

$$\text{for } k = 2 \;\Rightarrow\; \zeta_j = \mathcal{N}_j \text{ and } M = 1 \tag{41}$$

$$\text{for } k = 3 \;\Rightarrow\; \zeta_j = 1 \text{ and } M \neq 1 \tag{42}$$

Note that in the case $k = 3$, M is the overlap index of the partition of unity (number of nodes of the finite element).

Definition (40) is different from that proposed by [39], where the error estimator is obtained by summing the local functions $\boldsymbol{e}^{\omega_j}$ for each element over which the contributions of the norms are computed. The numerical examples presented by [48], in which the space $\mathcal{U}(\omega_j)$ is replaced by a finite but very refined approximate space, show that this strategy provides a more accurate error measure when compared with that of (40). However, [48] also show that for the computed version of the error estimator described below, both strategies (sum of the norms and norm of the sum of the local errors) can underestimate the error.

Note that definition (38) is simpler than (20). The error in the tractions, $\boldsymbol{t}(\tilde{\boldsymbol{u}})$, is not directly considered because the support of the local problem is a patch of elements, which implies that it includes the interelement faces. Therefore, the effect of the jumps in the traction across the element faces is implicitly accounted for, and there is no need to evaluate the traction jumps in the approximate solution, as observed by [15]. However, the presence of the function $\mathcal{N}_j$ in the residue expression nullifies any integration along the boundary of an inner patch. As there is no need to compute the tractions jumps along the element boundaries, no equilibration technique is necessary.

Measure (40) provides a theoretical upper estimator, as mentioned previously. The theoretical and computed error measures used in [3] are adopted here to differentiate the solution of (35) from that obtained with the Galerkin approximation, stated as:

Find $\tilde{\boldsymbol{e}}^{\omega_j}_{p+q} \in \mathcal{X}^0_{p+q}(\omega_j)$, such that

$$\mathcal{B}^{\zeta_j}_{\omega_j}(\tilde{\boldsymbol{e}}^{\omega_j}_{p+q}, \tilde{\boldsymbol{v}}_{p+q}) = \mathcal{R}_{\omega_j}(\mathcal{N}_j\tilde{\boldsymbol{v}}_{p+q}) \;\; \forall \;\; \tilde{\boldsymbol{v}}_{p+q} \in \mathcal{X}^0_{p+q}(\omega_j) \tag{43}$$

where the residual functional is defined as

$$\mathcal{R}_{\omega_j}(\mathcal{N}_j\tilde{\boldsymbol{v}}_{p+q}) = \mathcal{F}_{\omega_j}(\mathcal{N}_j\tilde{\boldsymbol{v}}_{p+q}) - \mathcal{B}_{\omega_j}(\tilde{\boldsymbol{u}}, \mathcal{N}_j\tilde{\boldsymbol{v}}_{p+q}) \tag{44}$$

and

$$\mathcal{B}^{\zeta_j}_{\omega_j}(\tilde{\boldsymbol{e}}^{\omega_j}_{p+q}, \tilde{\boldsymbol{v}}_{p+q}) = \iint_{\omega_j} \zeta_j \boldsymbol{\varepsilon}^T(\tilde{\boldsymbol{v}}_{p+q})\boldsymbol{\sigma}(\tilde{\boldsymbol{e}}^{\omega_j}_{p+q})\, d\Omega \tag{45}$$

$$\mathcal{F}_{\omega_j}(\mathcal{N}_j\tilde{\boldsymbol{v}}_{p+q}) = \iint_{\omega_j} (\mathcal{N}_j\tilde{\boldsymbol{v}}_{p+q})^T \boldsymbol{b}\, d\Omega + \int_{\partial\omega_j\cap\Gamma_N} (\mathcal{N}_j\tilde{\boldsymbol{v}}_{p+q})^T \hat{\boldsymbol{t}}\, d\Gamma \tag{46}$$

$$\mathcal{B}_{\omega_j}(\tilde{\boldsymbol{u}}, \mathcal{N}_j\tilde{\boldsymbol{v}}_{p+q}) = \iint_{\omega_j} \boldsymbol{\varepsilon}^T(\mathcal{N}_j\tilde{\boldsymbol{v}}_{p+q})\boldsymbol{\sigma}(\tilde{\boldsymbol{u}})\, d\Omega \tag{47}$$

for which

$$\mathcal{X}^0_{p+q}(\omega_j) = \{\tilde{\boldsymbol{v}}_{p+q} \in \mathcal{U}_{p+q}(\omega_j);\; \Pi_p(\tilde{\boldsymbol{v}}_{p+q}) = 0;\; \tilde{\boldsymbol{v}}_{p+q} = 0 \text{ on } \partial\omega_j \cap \Gamma_D\} \tag{48}$$

$$\tilde{\boldsymbol{e}}^{\omega_j}_{p+q} = (\boldsymbol{\Phi}^{\omega_j}_{p+q})^T \boldsymbol{I}^{\omega_j} \tag{49}$$

$$\tilde{\boldsymbol{v}}_{p+q} = (\boldsymbol{\Phi}^{\omega_j}_{p+q})^T \boldsymbol{V}^{\omega_j} \tag{50}$$

Here, the space $\mathcal{X}^0_{p+q}(\omega_j)$ and the functions $\tilde{\boldsymbol{e}}^{\omega_j}_{p+q}$ and $\tilde{\boldsymbol{v}}_{p+q}$ are defined analogously to (22), (28) and (28), respectively, but are extended to the set of elements that belong to the patch ω_j. Each component of $\left(\boldsymbol{\Phi}^{\omega_j}_{p+q}\right)^T = \left[\left(\boldsymbol{\phi}^{\omega_j}_{p+q}\right)^T_\alpha\right]^{N_{\omega_j}}_{\alpha=1}$ is given by:

$$\left(\boldsymbol{\phi}^{\omega_j}_{p+q}\right)^T_\alpha = \left[\mathcal{N}_\alpha(\boldsymbol{x})\, L^p_{\alpha k}(\bar{\boldsymbol{x}})\right]^{n^p_j+n^q_j}_{k=n^p_j+1} \tag{51}$$

and the vectors of parameters are

$$\left(\boldsymbol{I}^{\omega_j}\right)^T = \left[\left(\left[i^{\omega_\alpha}_k\right]^{n^p_j+n^q_j}_{k=n^p_j+1}\right)^T_\alpha\right]^{N_{\omega_j}}_{\alpha=1}$$

$$\left(\boldsymbol{V}^{\omega_j}\right)^T = \left[\left(\left[v^{\omega_\alpha}_k\right]^{n^p_j+n^q_j}_{k=n^p_j+1}\right)^T_\alpha\right]^{N_{\omega_j}}_{\alpha=1}$$

The difference is that these functions are associated with each one of the N_{ω_j} nodes $\boldsymbol{x}_\alpha$ covered by the patch ω_j rather than with those nodes belonging to a finite element $\mathcal{K}_E$. In Fig. 1a, for example, the patch ω_j cover $N_{\omega_j} = 9$ nodes.

Following definitions (40), (41) and (41), the computed error estimators are obtained by summing the local contributions of each patch and can underestimate the norm of the exact error:

$$\mathcal{E}_k = \sqrt{M}\sqrt{\sum_{j=1}^{N} ||\tilde{\boldsymbol{e}}^{\omega_j}_{p+q}||^2_{U(\omega_j)}} = \sqrt{M}\sqrt{\sum_{j=1}^{N} \mathcal{B}^{\zeta}_{\omega_j}(\tilde{\boldsymbol{e}}^{\omega_j}_{p+q}, \tilde{\boldsymbol{e}}^{\omega_j}_{p+q})} \tag{52}$$

The error indicators associated with the patches, with $k = 2$ or $k = 3$ can be defined as follows:

$$\mathcal{E}^{\omega_j}_k = \sqrt{M||\tilde{\boldsymbol{e}}^{\omega_j}_{p+q}||^2_{U(\omega_j)}} \tag{53}$$

In [39], the test functions used in the residual expression (44) are subtracted from the projection onto the finite element solution space to ensure the solvability of the error problem. This is imposed to verify the compatibility condition for the test functions with respect to the bilinear operator $\mathcal{B}_{\omega_j}(\cdot,\cdot)$. In this paper, this condition is guaranteed by using the "patch-bubble" space $\mathcal{X}^0_{p+q}(\omega_j)$ defined in (48).

According to [43], a lower estimator associated with each subdomain error measure can be obtained by recovering continuous estimates of the error functions. For the error estimators discussed here, the lower estimator is given by:

$$\mathcal{E}^L_k = \frac{(\mathcal{E}_k)^2}{M\|z(\boldsymbol{x})\|_U} \tag{54}$$

where $z(\boldsymbol{x})$ is the continuous function given by:

$$z(\boldsymbol{x}) = \sum_{j=1}^{N} \mathcal{N}_j(\boldsymbol{x})\tilde{\boldsymbol{e}}^{\omega_j}_{p+q}(\boldsymbol{x}) \tag{55}$$

and

$$\|z\|^2_U = \mathcal{B}(z,z) = \iint_{\Omega} \boldsymbol{\varepsilon}^T(z)\boldsymbol{\sigma}(z)\, d\Omega \tag{56}$$

is the energy norm calculated over the entire domain Ω. Note that the function $z(\boldsymbol{x})$ is continuous because the PoU $\mathcal{N}_j(\boldsymbol{x})$ vanishes at the boundaries of all patches and $\tilde{\boldsymbol{e}}^{\omega_j}_{p+q}(\boldsymbol{x})$, the solution of (43), is continuous within the patch ω_j.

4.3 Implicit subdomain residual method—an alternative strategy

In the implicit subdomain residual method presented in the previous section, the global equation (15) for the error is decomposed into patch contributions by introducing the PoU functions into the residual functional (34). In this section, an alternative strategy is proposed, in which the products of the PoU functions and test functions are introduced as weights in

the weighted-integral statement of the differential equation of the error problem, as follows.

Consider the following integral form given by the weighted residual method:

Find $\boldsymbol{e} \in \mathcal{U}(\Omega)$, such that

$$\int_{\Omega} \left(\sum_{j=1}^{N} \mathcal{N}_j \boldsymbol{v} \right) \{ \nabla \cdot \boldsymbol{\sigma}(\boldsymbol{e}) + \boldsymbol{r}_{\Omega} \} \, d\Omega = 0 \;\; \forall \;\; \boldsymbol{v} \in \mathcal{U}(\Omega) \quad (57)$$

where $\boldsymbol{r}_{\Omega}$ is the residue of differential equation (4) if the solution $\boldsymbol{u}$ is replaced by its GFEM approximation, $\tilde{\boldsymbol{u}}$:

$$\boldsymbol{r}_{\Omega} = \nabla \cdot \boldsymbol{\sigma}(\tilde{u}) + \boldsymbol{b} \quad (58)$$

Using the PoU properties, this problem can be decomposed into more restrictive local problems:

Find $\boldsymbol{e}^{\omega_j} \in \mathcal{U}(\omega_j)$, such that

$$\int_{\omega_j} \left(\mathcal{N}_j \boldsymbol{v} \right) \left\{ \nabla \cdot \boldsymbol{\sigma}(\boldsymbol{e}^{\omega_j}) + \boldsymbol{r}_{\Omega} \right\} d\Omega = 0 \; \forall \; \boldsymbol{v} \in \mathcal{V}(\omega_j) \quad (59)$$

which results, after applying the Gauss Theorem, in the final form of the local problem:

Find $\boldsymbol{e}^{\omega_j} \in \mathcal{U}(\omega_j)$, such that:

$$\mathcal{B}_{\omega_j}(\boldsymbol{e}^{\omega_j}, \mathcal{N}_j \boldsymbol{v}) = \mathcal{R}_{\omega_j}(\mathcal{N}_j \boldsymbol{v}) \;\; \forall \; \boldsymbol{v} \in \mathcal{V}(\omega_j) \quad (60)$$

where the residual functional is the same of (36) and

$$\mathcal{B}_{\omega_j}(\boldsymbol{e}^{\omega_j}, \mathcal{N}_j \boldsymbol{v}) = \int_{\omega_j} \boldsymbol{\varepsilon}^T \left(\mathcal{N}_j \boldsymbol{v} \right) \boldsymbol{\sigma}(\boldsymbol{e}^{\omega_j}) \, d\Omega \quad (61)$$

As in the previous sections, the computed version of this problem can be obtained using the following Galerkin approximation:

Find $\tilde{\boldsymbol{e}}^{\omega_j}_{p+q} \in \mathcal{X}^0_{p+q}(\omega_j)$, such that

$$\mathcal{B}_{\omega_j}(\tilde{\boldsymbol{e}}^{\omega_j}_{p+q}, \mathcal{N}_j \tilde{\boldsymbol{v}}_{p+q}) = \mathcal{R}_{\omega_j}(\mathcal{N}_j \tilde{\boldsymbol{v}}_{p+q}) \quad \forall \; \tilde{\boldsymbol{v}}_{p+q} \in \mathcal{X}^0_{p+q}(\omega_j) \quad (62)$$

and

$$\mathcal{B}_{\omega_j}(\tilde{\boldsymbol{e}}^{\omega_j}_{p+q}, \mathcal{N}_j \tilde{\boldsymbol{v}}_{p+q}) = \int_{\omega_j} \boldsymbol{\varepsilon}^T \left(\mathcal{N}_j \tilde{\boldsymbol{v}}_{p+q} \right) \boldsymbol{\sigma}(\tilde{\boldsymbol{e}}^{\omega_j}_{p+q}) d\Omega \quad (63)$$

Here, the residual function is given by (44) and the space $\mathcal{X}^0_{p+q}(\omega_j)$ and the functions $\tilde{\boldsymbol{e}}^{\omega_j}_{p+q}$ and $\tilde{\boldsymbol{v}}_{p+q}$ have the same definitions (48), (49) and (50), respectively. Differently from (45), the bi-linear form (63) is not symmetric, due to the presence of the PoU directly multiplying the test functions. The computed versions of the error estimator and error indicator are given by:

$$\mathcal{E}_4 = \sqrt{\sum_{j=1}^{N} \left| \mathcal{B}_{\omega_j}(\tilde{\boldsymbol{e}}^{\omega_j}_{p+q}, \mathcal{N}_j \tilde{\boldsymbol{e}}^{\omega_j}_{p+q}) \right|} \quad (64)$$

$$\mathcal{E}_4^{\omega_j} = \sqrt{\left| \mathcal{B}_{\omega_j}(\tilde{\boldsymbol{e}}^{\omega_j}_{p+q}, \mathcal{N}_j \tilde{\boldsymbol{e}}^{\omega_j}_{p+q}) \right|} \quad (65)$$

A strategy similar to the one given in Sect. 4.2, is used here to propose a lower estimator, i.e., using in (54) and (55) and the function obtained with the solution of the problem (62).

5 Numerical examples

Numerical examples are used to evaluate the performance of the four types of error estimators—$\mathcal{E}_1$ of Eq. (32), $\mathcal{E}_2$ and $\mathcal{E}_3$ of Eq. (52) and $\mathcal{E}_4$ of Eq. (64), summarized in Table 1. Two-dimensional elasticity problems with smooth and non-smooth solutions are solved using h and p-refinement strategies. The h-refinement adopted employs a uniform division of the mesh. The p-refinement is also uniform and is achieved using the enrichment strategy described in Sect. 2 by replacing the functions $\left\{ L^p_{jk}(\bar{\boldsymbol{x}}) \right\}_{k=1}^{n_j^p}$ of the set $\mathcal{I}_j$ defined in (1) by the polynomials required to construct the polynomial basis of the approximation. Particular attention is given to the last two examples, with singular points located on the boundary of the solution domain. These are the points at which the stress field is singular, e.g., the concave of the boundary and the crack tip. In these problems, functions that can reproduce this singular stress field are also added to the set of functions $\mathcal{I}_j$, corresponding to $\left\{ L^s_{jl}(\boldsymbol{x}) \right\}_{l=1}^{n_j^s}$. These functions are referred to here as *special*, and the enrichment strategies are referred to as *special*-enrichment. Even when *special*-enrichment is used to construct the approximate solution together with of p-enrichment, the approximate error is still polynomial and it is described by functions of the spaces $\mathcal{X}^0_{p+q}(\mathcal{K}_E)$, with $q = 1, 2$, for estimator $\mathcal{E}_1$ and $\mathcal{X}^0_{p+q}(\omega_j)$, with $q = 1, 2$ for the other three estimators as well.

A Gauss quadrature rule is used to perform, when possible, a precise numerical integration of the solution and error problems. Different numbers of integration points are adopted for each problem and type of enrichment strategy. In problems with non-smooth solutions, the numerical integrations are performed with 100×100 points for patches of elements enriched by *special* functions (with singular derivatives). This procedure should not be adopted in practical analysis, but it minimizes the numerical integration error here.

The error estimators are evaluated based on two indices:

– the effectivity index, θ, that is, the ratio between the error measure and the analytical or reference error in the energy norm $\|\boldsymbol{e}\|_U$.

$$\theta_k = \frac{\mathcal{E}_k}{\|\boldsymbol{e}(\boldsymbol{x})\|_U} \qquad \theta_k^L = \frac{\mathcal{E}_k^L}{\|\boldsymbol{e}(\boldsymbol{x})\|_U} \quad (66)$$

Table 1 Analytical expressions adopted for the error measures—with $z(\boldsymbol{x}) = \sum_{j=1}^{N} \mathcal{N}_j(\boldsymbol{x}) \tilde{\boldsymbol{e}}_{p+q}^{\omega_j}(\boldsymbol{x})$ from (55), and $M = 4$ for quadrilateral elements

Error measure	Expression
$\mathcal{E}_1$	$\sqrt{\sum_{\mathcal{K}_E \in \Omega} \left[\mathcal{B}_{\mathcal{K}_E}(\tilde{\boldsymbol{e}}_{p+q}^{\mathcal{K}_E}, \tilde{\boldsymbol{e}}_{p+q}^{\mathcal{K}_E}) \right]}$
$\mathcal{E}_2$	$\sqrt{\sum_{j=1}^{N} \mathcal{B}_{\omega_j}^{\zeta=\mathcal{N}_j}(\tilde{\boldsymbol{e}}_{p+q}^{\omega_j}, \tilde{\boldsymbol{e}}_{p+q}^{\omega_j})}$
$\mathcal{E}_2^I$	$\dfrac{(\mathcal{E}_2)^2}{\mathcal{B}(z,z)}$
$\mathcal{E}_3$	$\sqrt{M \sum_{j=1}^{N} \mathcal{B}_{\omega_j}^{\zeta=1}(\tilde{\boldsymbol{e}}_{p+q}^{\omega_j}, \tilde{\boldsymbol{e}}_{p+q}^{\omega_j})}$
$\mathcal{E}_3^I$	$\dfrac{(\mathcal{E}_3)^2}{M\mathcal{B}(z,z)}$
$\mathcal{E}_4$	$\sqrt{\sum_{j=1}^{N} \left\lvert \mathcal{B}_{\omega_j}(\tilde{\boldsymbol{e}}_{p+q}^{\omega_j}, \mathcal{N}_j \tilde{\boldsymbol{e}}_{p+q}^{\omega_j}) \right\rvert}$
$\mathcal{E}_4^I$	$\dfrac{(\mathcal{E}_4)^2}{\mathcal{B}(z,z)}$

– the robustness index, ρ, corresponding to the ratio between the error measure and the lower error estimator, if available.

$$\rho_k = \frac{\mathcal{E}_k}{\mathcal{E}_k^L} \tag{67}$$

The orthogonality property of the Galerkin approximation makes it possible to use the following expression to calculate the energy norm of the error:

$$\|\boldsymbol{e}(\boldsymbol{x})\|_U^2 = \|\boldsymbol{u}(\boldsymbol{x})\|_U^2 - \|\tilde{\boldsymbol{u}}(\boldsymbol{x})\|_U^2 \tag{68}$$

In problems where the analytical solution is unknown, the norm $\|\boldsymbol{u}(\boldsymbol{x})\|_U$ is replaced by the energy norm of a so-called reference solution. This reference solution is obtained using a highly refined mesh and p extrapolation, following [50]. The analytical or reference solution is also used to calculate the relative error, given by:

$$\eta = \frac{\|\boldsymbol{e}(\boldsymbol{x})\|_U}{\|\boldsymbol{u}(\boldsymbol{x})\|_U} \tag{69}$$

The effectivity and robustness indices are associated with the number of degrees of freedom (NDOF) or the polynomial degree p of the approximation in the case of h- or p-refinement, respectively.

5.1 Linear bending problem

In Fig. 2a, the description and data of a two-dimensional plane stress problem are presented, where the loading is described by the following equations:

$$q_x = \frac{240y}{c} - 120 \tag{70}$$

$$q_y = \frac{120y}{L} - \frac{120y^2}{cL} \tag{71}$$

The exact analytical solution to this classical elasticity problem can be found in [28], and the exact strain energy is 0.080624. The problem is solved using meshes of quadrangular elements with linear ($p = 1$) approximations. The enrichment strategy is not intended to be used here for the approximate solution, but only for constructing the error indicators.

To evaluate the convergence of the global effectivity index as the approximation is improved, three meshes were considered, as illustrated in Fig. 2b–d. The effectivity indices are shown in Table 2, along with the exact relative errors in the energy norm. Plots of the effectivity and robustness indices are shown in Fig. 3. The error function is projected onto $\mathcal{X}_{p+1}^0(\mathcal{K}_E)$ for estimator $\mathcal{E}_1$ and $\mathcal{X}_{p+1}^0(\omega_j)$ for the other three estimators.

All four types of estimators tend to fall near unity for both the effectivity and robustness indices, when available. Only the estimators $\mathcal{E}_2$ and $\mathcal{E}_3$ tend to be upper bounds as the relative error decreases.

5.2 Plate with a circular hole

The problem of an infinite plate with a circular hole, in the plane strain state and subjected to a unidirectional tension σ_∞, is illustrated in Fig. 4a. A mesh with twelve quadrangular elements is used to construct the PoU linear functions, as shown in Fig. 4b. The analysis is performed over the domain ABCDEA of Fig. 4a. The p-refinement is performed using the enrichment strategy of Sect. 2. Symmetry conditions are imposed on edges AB and DE. To represent the curved boundary EA, the linear blending function method proposed in [24] was adopted. The following stress distribution, obtained from the elastic solution of [51] (which leads to a strain energy of 7.6936442), is imposed on edges BC and CD:

$$\sigma_x = \sigma_\infty \left[1 - \frac{a^2}{r^2} \left(\frac{3}{2} \cos 2\theta + \cos 4\theta \right) + \frac{3a^4}{2r^4} \cos 4\theta \right] \tag{72}$$

$$\sigma_y = \sigma_\infty \left[-\frac{a^2}{r^2} \left(\frac{1}{2} \cos 2\theta - \cos 4\theta \right) - \frac{3a^4}{2r^4} \cos 4\theta \right] \tag{73}$$

$$\tau_{xy} = \sigma_\infty \left[-\frac{a^2}{r^2} \left(\frac{1}{2} \operatorname{sen} 2\theta + \cos 4\theta \right) + \frac{3a^4}{2r^4} \cos 4\theta \right] \tag{74}$$

The effectivity indices for the four estimators are presented in Table 3. Plots of the effectivity and robustness indices are shown in Fig. 5. The error function is projected

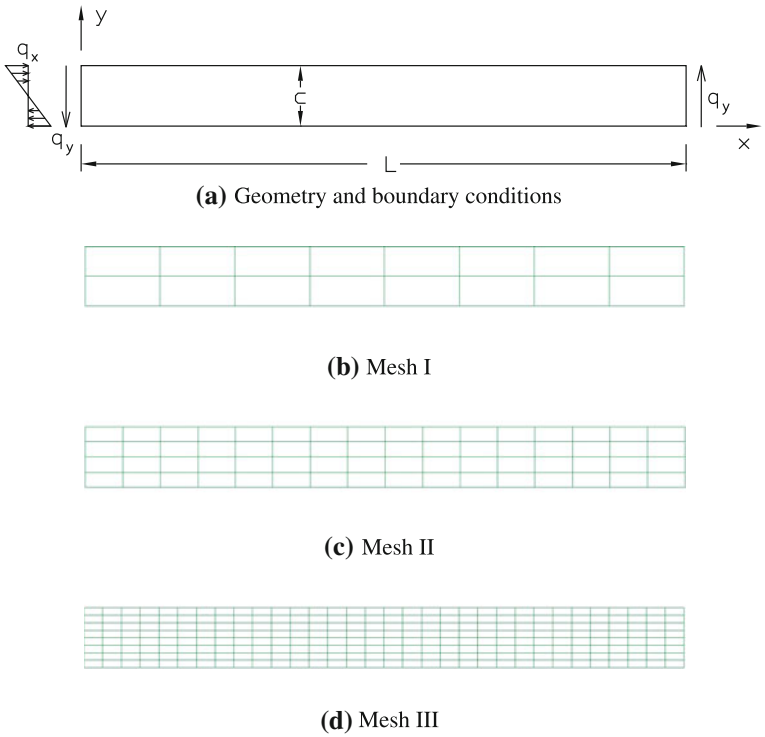

(a) Geometry and boundary conditions

(b) Mesh I

(c) Mesh II

(d) Mesh III

Fig. 2 Geometry and discretization. Young's modulus $E = 1 \times 10^7$, Poisson coefficient $\nu = 0.3$, thickness 1.0, $L = 100$ and $c = 10$

Table 2 Global effectivity indices and relative error

Mesh	NDOF	$\mathcal{E}_1$	$\mathcal{E}_2$	$\mathcal{E}_2^l$	$\mathcal{E}_3$	$\mathcal{E}_3^l$	$\mathcal{E}_4$	$\mathcal{E}_4^l$	η (%)
I	51	0.814	0.867	0.758	0.843	0.772	0.793	0.792	62.09
II	167	0.944	1.003	0.905	0.967	0.909	0.938	0.814	36.71
III	584	0.987	1.049	0.963	1.009	0.963	0.982	0.954	19.38

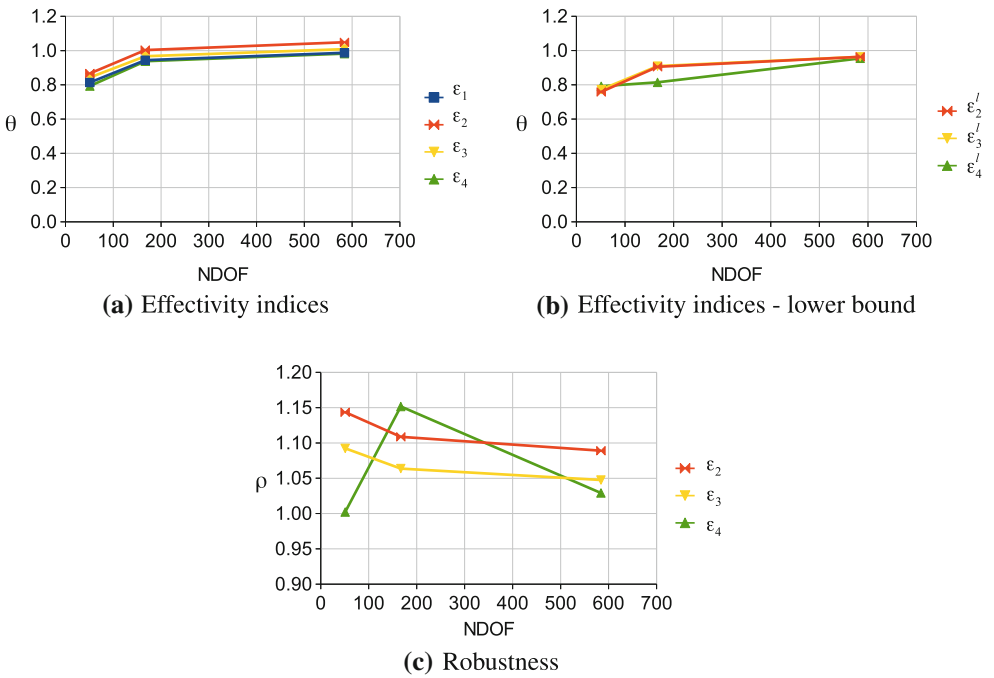

(a) Effectivity indices

(b) Effectivity indices - lower bound

(c) Robustness

Fig. 3 Effectivity and robustness indices

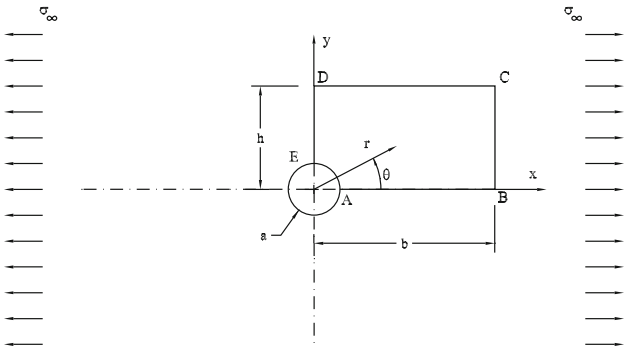

(a) Geometry and boundary conditions

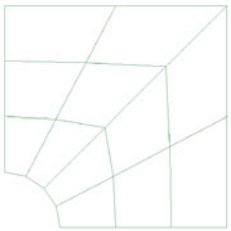

(b) Mesh

Fig. 4 Geometry and discretization. $a = 1.0$, $b = h = 4.0$, Young's modulus $E = 1.0$, Poisson coefficient $\nu = 0.3$, thickness $t = 1.0$ and $\sigma_\infty = 1.0$

onto $\mathcal{X}^0_{p+1}(\mathcal{K}_E)$ for the estimator $\mathcal{E}_1$ and $\mathcal{X}^0_{p+1}(\omega_j)$ for the other three estimators.

The computed estimators $\mathcal{E}_1$, $\mathcal{E}_2$ and $\mathcal{E}_3$ exhibit good performance, and the effectivity and robustness indices (in the case of the latter two) are close to unity. The third estimator displays an upper bound behavior, except for the analysis with $p = 4$. In this analysis, the relative error is lower than one percent, and the error measure is most likely polluted by round-off errors, iteration error of the linear system solver and/or error caused by the numerical integration. Despite converging to an upper bound, the estimator $\mathcal{E}_4$ has a lower bound that severely underestimates the error.

Table 3 Global effectivity indices

p	$\mathcal{E}_1$	$\mathcal{E}_2$	$\mathcal{E}_2^l$	$\mathcal{E}_3$	$\mathcal{E}_3^l$	$\mathcal{E}_4$	$\mathcal{E}_4^l$	η (%)
1	0.868	1.219	0.571	1.125	0.705	0.804	0.391	14.51
2	0.971	1.046	0.729	1.136	0.826	1.393	0.218	6.20
3	0.973	0.978	0.868	1.112	0.819	1.225	0.100	2.47
4	0.948	0.920	0.819	0.905	0.740	1.112	0.060	0.87

5.3 L-shape plate

Consider the following problem, described by [50] and depicted in Fig. 6. A plate in the plane strain state is subjected to the following stress field along edges AB, BC, EF and FA corresponding to the Mode 1 term of the asymptotic expansion of the displacement field around the vertex D:

$$\sigma_x = A_1\lambda_1 r^{\lambda_1-1}\{[2 - Q_1(\lambda_1+1)]\cos(\lambda_1-1)\theta - (\lambda_1-1)\cos(\lambda_1-3)\theta\} \quad (75)$$

$$\sigma_y = A_1\lambda_1 r^{\lambda_1-1}\{[2 + Q_1(\lambda_1+1)]\cos(\lambda_1-1)\theta + (\lambda_1-1)\cos(\lambda_1-3)\theta\} \quad (76)$$

$$\tau_{xy} = A_1\lambda_1 r^{\lambda_1-1}\{(\lambda_1-1)\,\text{sen}\,(\lambda_1-3)\theta$$

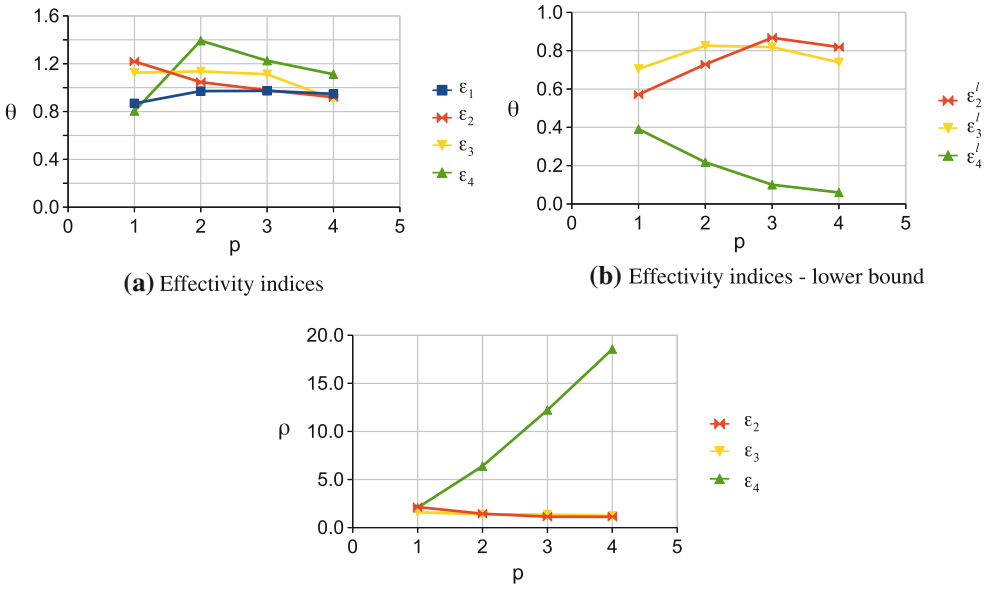

(a) Effectivity indices

(b) Effectivity indices - lower bound

(c) Robustness indices

Fig. 5 Global effectivity and robustness indices

Fig. 7 Discretization

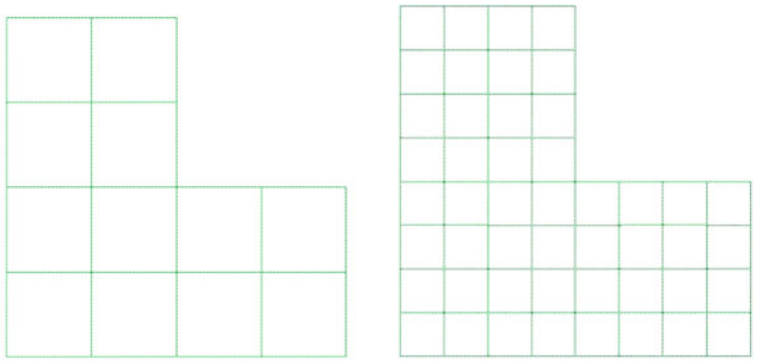

(a) Mesh I - 12 elements **(b)** Mesh II - 48 elements

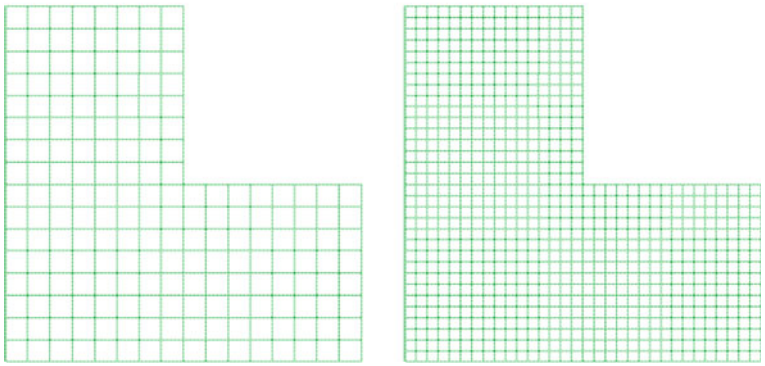

(c) Mesh III - 192 elements **(d)** Mesh IV - 768 elements

$$+ Q_1 (\lambda_1 + 1) \operatorname{sen} (\lambda_1 - 1)\theta\} \tag{77}$$

which corresponds to a displacement field given by the components u_x and u_y, as follows:

$$u_x = \frac{A_1}{2G} r^{\lambda_1} \{[\kappa - Q_1 (\lambda_1 + 1)] \cos \lambda_1 \theta - \lambda_1 \cos (\lambda_1 - 2)\theta\} \tag{78}$$

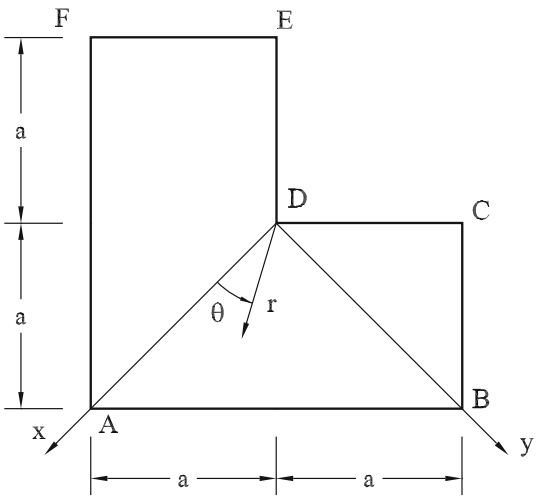

Fig. 6 Geometry. $a = 0.5$, Young's modulus $E = 1.0$, Poisson coefficient $\nu = 0.3$, thickness 1.0

$$u_y = \frac{A_1}{2G} r^{\lambda_1} \{[\kappa + Q_1 (\lambda_1 + 1)] \operatorname{sen} \lambda_1 \theta + \lambda_1 \operatorname{sen} (\lambda_1 - 2)\theta\} \tag{79}$$

with $\lambda_1 = 0.544483737$, $Q_1 = 0.543075579$, $\kappa = 3 - 4\nu$, $A_1 = 1.0$, $G = \dfrac{E}{2(1+\nu)}$. The exact strain is 1.95301842.

In this problem, the stress field is singular at point D in Fig. 6. The strength of the singularity is described by the parameter λ_1. The effect of this singularity on the error measures is evaluated here for both h- and p-refinements. The h-refinement is performed using a sequence of meshes of quadrangular elements with linear ($p = 1$) approximations, represented in Fig. 7. In contrast, the p-refinement is conducted on mesh II of Fig. 7b, and the enrichment strategy is as described in Sect. 2. The corresponding effectivity indices of the four error estimators are shown in Tables 4 and 5. The plot in Fig. 8 also includes the robustness indices. The error functions are projected onto a larger space than those of Sects. 5.1 and 5.2 – $\mathcal{X}^0_{p+2}(\mathcal{K}_E)$ for estimator $\mathcal{E}_1$ and $\mathcal{X}^0_{p+2}(\omega_j)$ for the other three estimators. Projecting the error in $\mathcal{X}^0_{p+1}(\mathcal{K}_E)$ and $\mathcal{X}^0_{p+1}(\omega_j)$ as in the previous sections produced poor results for the effectivity indices; these results are not shown here.

Table 4 Global effectivity indices—*h* refinement

Mesh	NDOF	$\mathcal{E}_1$	$\mathcal{E}_2$	$\mathcal{E}_2^l$	$\mathcal{E}_3$	$\mathcal{E}_3^l$	$\mathcal{E}_4$	$\mathcal{E}_4^l$	η (%)
I	39	1.120	1.111	0.751	1.314	0.735	0.957	0.296	30.38
II	127	1.152	1.143	0.781	1.359	0.765	0.978	0.313	22.26
III	447	1.170	1.164	0.800	1.387	0.784	0.986	0.332	15.81
IV	1663	1.150	1.145	0.790	1.366	0.774	0.979	0.324	11.05

Table 5 Global effectivity indices—*p*-refinement

p	$\mathcal{E}_1$	$\mathcal{E}_2$	$\mathcal{E}_2^l$	$\mathcal{E}_3$	$\mathcal{E}_3^l$	$\mathcal{E}_4$	$\mathcal{E}_4^l$	η (%)
1	1.152	1.143	0.781	1.359	0.765	0.978	0.313	22.26
2	1.428	1.058	0.857	1.308	0.836	1.758	0.252	15.44
3	1.338	0.960	0.840	1.273	0.793	0.852	0.319	12.39
4	1.350	0.899	0.788	1.205	0.758	0.659	0.110	10.43

5.3.1 Space enriched with exact solution

The same sequence of *h*- and *p*-refinements is performed with the solution space enriched with the solutions u_x (78) and u_y (79) (taken as *special*-enrichment). In this case, the set $\mathcal{I}_j$ defined in (1) is improved as proposed by [7] by adding:

$$\left\{{}^{x}L^{s}_{jl}(\boldsymbol{x})\right\}_{l=1} = \left\{1 - \frac{u_x(\boldsymbol{x})}{u_x(\boldsymbol{x}_j)}\right\} \tag{80}$$

$$\left\{{}^{y}L^{s}_{jl}(\boldsymbol{x})\right\}_{l=1} = \left\{1 - \frac{u_y(\boldsymbol{x})}{u_y(\boldsymbol{x}_j)}\right\} \tag{81}$$

where j is the index of the node $\boldsymbol{x}_j$ whose patch has the PoU multiplied by the functions of $\mathcal{I}_j$. Figure 9 shows the sequence of meshes used in the *h*-refinement. The superscript x and y refer to the set of functions used to enrich components $\boldsymbol{u}_x$ and $\boldsymbol{u}_y$, respectively. Note that Expressions (80) and (81) are normalized to become null at $\boldsymbol{x} = \boldsymbol{x}_j$ enabling the direct imposition of the essential boundary conditions.

For each mesh, the enriched region using *special*-enrichment is illustrated in Fig. 9. Only those patches that are completely immersed in the shaded regions have their PoUs multiplied by the sets (80) and (81) in the x and y direction, respectively. In mesh II, for example, only the node at which the stress field is singular is enriched. Note that together with

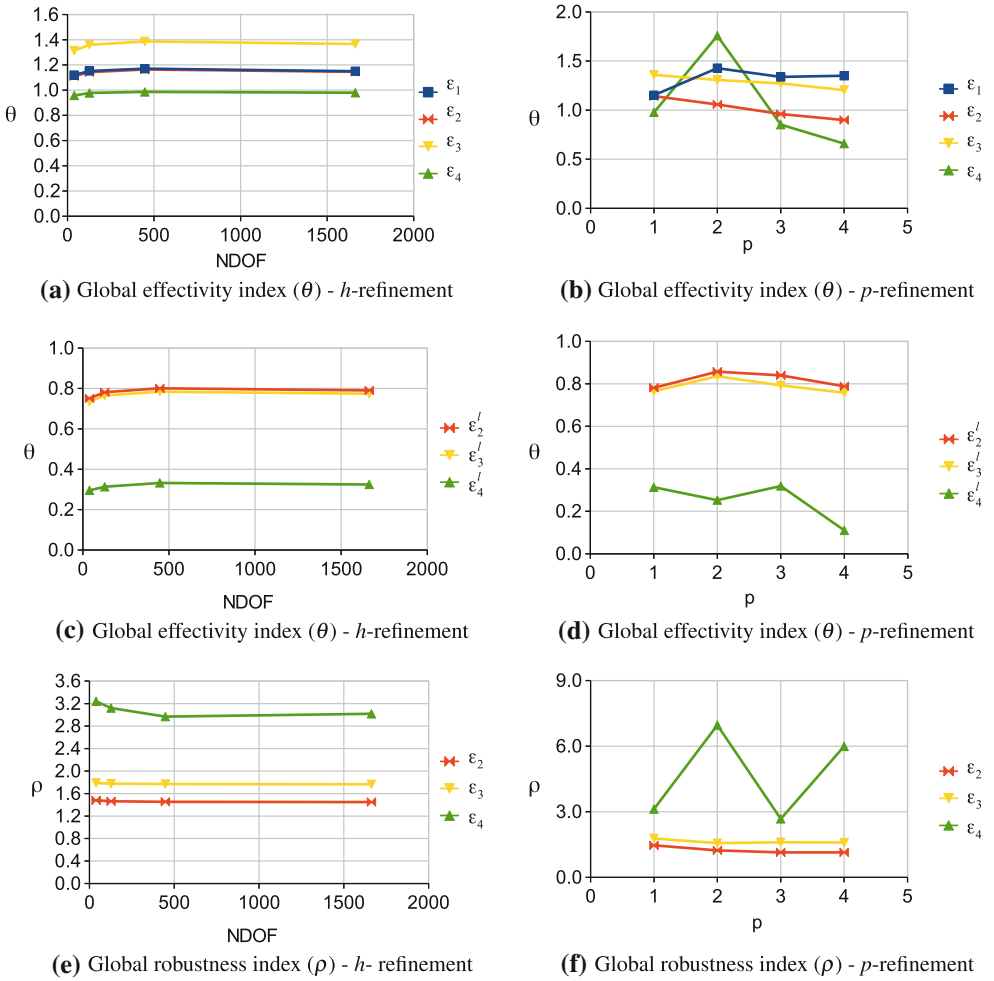

(a) Global effectivity index (θ) - *h*-refinement

(b) Global effectivity index (θ) - *p*-refinement

(c) Global effectivity index (θ) - *h*-refinement

(d) Global effectivity index (θ) - *p*-refinement

(e) Global robustness index (ρ) - *h*- refinement

(f) Global robustness index (ρ) - *p*-refinement

Fig. 8 Global effectivity (θ) and robustness (ρ) indices

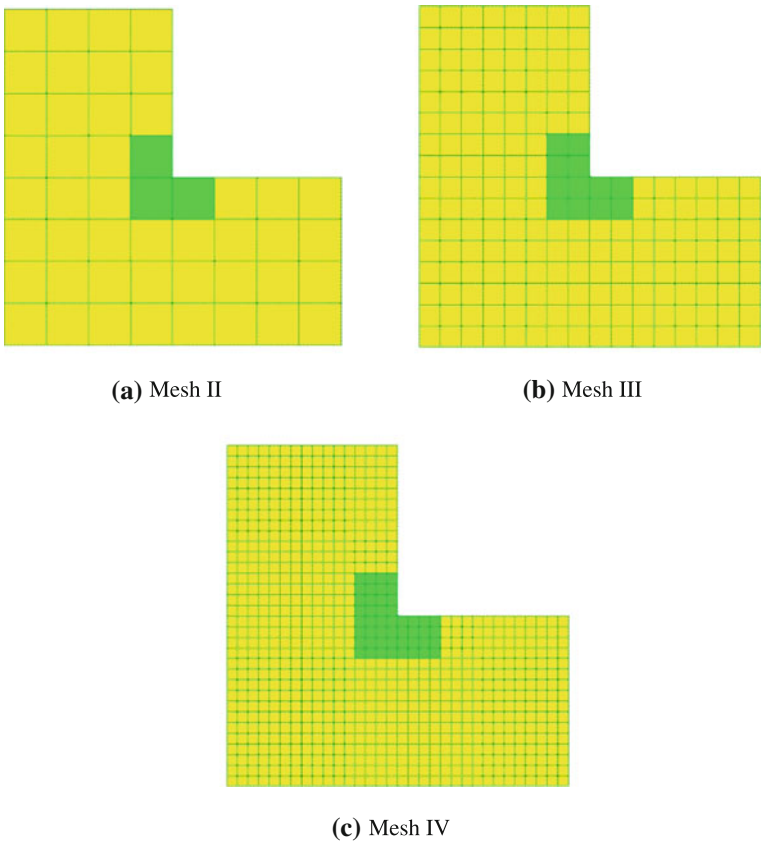

(a) Mesh II **(b)** Mesh III

(c) Mesh IV

Fig. 9 Region with *special*-enrichment

the h-refinement, a so-called geometric *special*-enrichment is performed. The p-refinement is executed on mesh II of Fig. 9a. Tables 6 and 7 and Fig. 10 show the effectivity and robustness indices obtained for the four error estimators.

For the $\mathcal{E}_2$ and $\mathcal{E}_3$ measures, there is significant improvement in the effectivity and robustness indices when *special*-enrichment is employed. When the *special*-enrichment is used, the effectivity indices are closer to the upper bound, and the robustness indices are closer to unity. This behavior is expected as the *special*-enrichment can describe the singular stress field, improving the approximate solution. Then, only the smooth part of the solution must be approximated by the h- or p-refinements. It is this smooth part that is estimated when the error is projected onto the space $\mathcal{X}^0_{p+q}(\omega_j)$ of problem (43). As $\mathcal{X}^0_{p+q}(\omega_j)$ is a polynomial space, the resulting estimators are closer to the exact error than in the case without *special*-enrichment. When only h- or p-refinement is performed, the non-smooth portion of the error cannot be adequately approximated by the functions in space $\mathcal{X}^0_{p+q}(\omega_j)$. For the same reason, the estimator $\mathcal{E}_1$ achieves more precise values and an upper bound behavior. The estimator $\mathcal{E}_4$ also exhibits an improvement in the indices when *special*-enrichment is added. However, very small values are obtained for its lower bound version, which explains the poor results for the robustness indices.

Table 6 Global effectivity indices—h-refinement and *special*-enrichment

Mesh	NDOF	$\mathcal{E}_1$	$\mathcal{E}_2$	$\mathcal{E}_2^l$	$\mathcal{E}_3$	$\mathcal{E}_3^l$	$\mathcal{E}_4$	$\mathcal{E}_4^l$	η (%)
II	143	1.010	1.153	0.882	1.255	0.845	1.066	0.164	10.38
III	489	1.012	1.152	0.915	1.285	0.869	0.993	0.155	6.24
IV	1793	1.015	1.156	0.940	1.311	0.887	0.962	0.157	3.51

Table 7 Global effectivity indices—p-refinement and *special*-enrichment

p	$\mathcal{E}_1$	$\mathcal{E}_2$	$\mathcal{E}_2^l$	$\mathcal{E}_3$	$\mathcal{E}_3^l$	$\mathcal{E}_4$	$\mathcal{E}_4^l$	η (%)
1	1.010	1.153	0.882	1.255	0.845	1.066	0.164	10.50
2	1.065	1.112	0.955	1.419	0.922	1.971	0.300	1.40
3	1.131	1.072	0.958	1.444	0.914	0.917	0.224	0.71
4	1.447	1.043	0.953	1.448	0.931	1.149	0.086	0.21

5.3.2 *Performance of error indicators*

To evaluate how the *special*-enrichment affects the quality of the local error estimates, the corresponding error indicators are analyzed. Note that, in general, all of the estimators exhibit similar relative performance when comparing refinements with and without *special*-enrichment. Slightly better results for both types of refinement are observed with the esti-

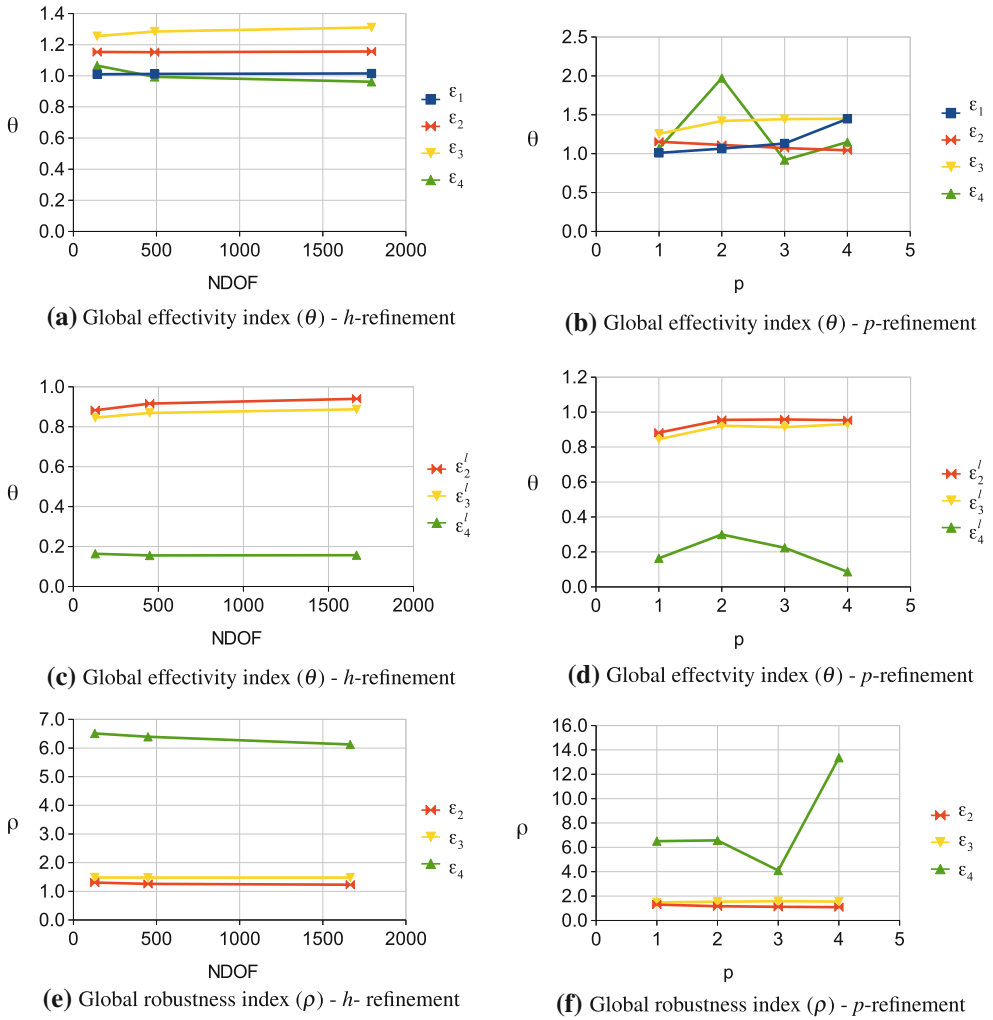

(a) Global effectivity index (θ) - h-refinement

(b) Global effectivity index (θ) - p-refinement

(c) Global effectivity index (θ) - h-refinement

(d) Global effectvity index (θ) - p-refinement

(e) Global robustness index (ρ) - h- refinement

(f) Global robustness index (ρ) - p-refinement

Fig. 10 Global effectivity (θ) and robustness (ρ) indices—solution space with *special*-enrichment

mator $\mathcal{E}_3$. The $\mathcal{E}_3$ estimator was therefore chosen to illustrate the error indicator behavior. Figure 11 shows the distribution of the local effectivity indices. The local effectivity index refers to the ratio between the error indicator, given by Eq. (53), and the corresponding norm using the analytical error. The local index is calculated for each patch, and its value is interpolated over the elements. The analysis performed with Mesh II was selected. First, the error indicators are compared when the solution is constructed using $p = 4$-enrichment, with or without *special*-enrichment, as shown in Fig. 11a, b, respectively. Note that the range of the local effectivity index is narrower when *special*-enrichment is included in the approximate solution space. The overall behavior of the error is illustrated in Fig. 12, which shows the distribution of the energy norm of the exact error. In addition to the decrease in the error, a wider distribution is observed in the region of *special*-enrichment. To compare problems with equivalent relative errors, the problem of Fig. 11a can be used together with that of Fig. 11c, with $p = 1$ and *special*-enrichment. In this case, the local effectivity index distribution does not exhibit the same uniformity as in Fig. 11b but still has a narrower range of variation when compared to Fig. 11a.

5.4 Plate with a crack

Consider a cracked plate in the plane stress state, subjected to a tensile stress such that the opening mode predominates, as shown in Fig. 13(a). The presence of the crack produces a stress field with a stronger singularity than that observed in the problem of Sect. 5.3. The effects of this singularity on the estimators $\mathcal{E}_1$, $\mathcal{E}_2$, $\mathcal{E}_3$ and $\mathcal{E}_4$ are evaluated using solution spaces analogous to those defined in (80) and (81) in Sect. 5.3. The functions used in the *special*-enrichment are given by Eqs. (78) and (79), with $\lambda_1 = 0.5$ and $Q_1 = 1/3$. Those functions are referred to by [40] as OD branch functions, from [35], and compared to the BB branch functions of [9]. In contrast to the calculations in Sect. 5.3, here these sets of functions multiply only the PoU associated with the

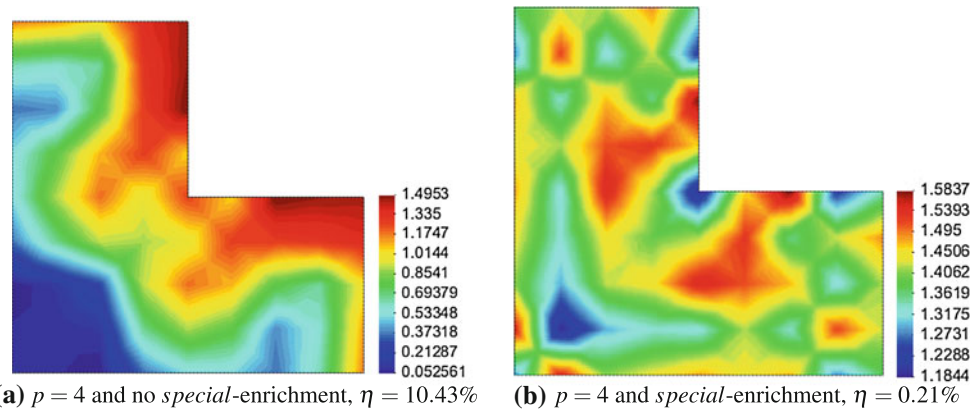

(a) $p = 4$ and no *special*-enrichment, $\eta = 10.43\%$ **(b)** $p = 4$ and *special*-enrichment, $\eta = 0.21\%$

(c) $p = 1$ and *special*-enrichment, $\eta = 10.50\%$

Fig. 11 Local effectivity indices distribution—estimator $\mathcal{E}_3$-Mesh II (graphical representation using [13])

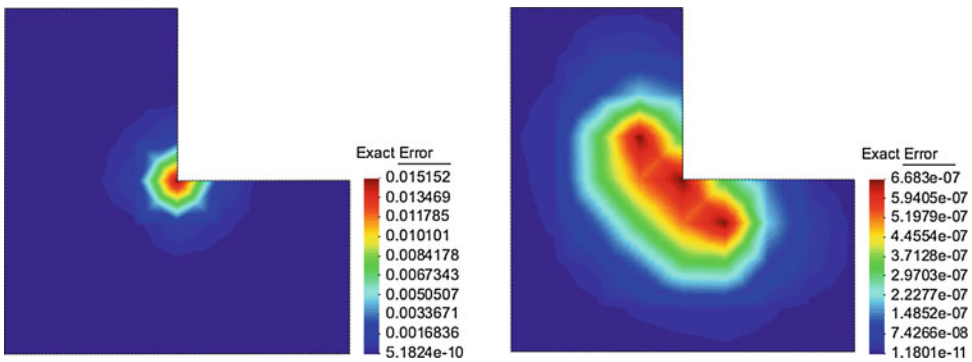

(a) $p = 4$ and no *special*-enrichment, $\eta = 10.43\%$ **(b)** $p = 4$ and *special*-enrichment, $\eta = 0.21\%$

Fig. 12 Exact error—Energy norm distribution—Mesh II—(graphical representation using [13])

node at the crack tip. The adopted mesh has 25 elements and is depicted in Fig. 13b.The reference strain energy of 5.49163373 is obtained for a mesh with 12,087 elements and $(p = 1, 2, 3)$-extrapolation, resulting in 24,624, 73,422 and 122,240 degrees of freedom respectively.

Tables 8 and 9 and Fig. 14 show the relative errors, effectivity and robustness indices for the two p-refinement strategies: with and without *special*-enrichment. The error function is projected onto $\mathcal{X}^0_{p+1}(\mathcal{K}_E)$ for estimator $\mathcal{E}_1$ and $\mathcal{X}^0_{p+1}(\omega_j)$ for the other three estimators. Note that the estimators $\mathcal{E}_1$, $\mathcal{E}_2$ and $\mathcal{E}_3$ exhibit good performance primarily for p-refinement and *special*-enrichment. In these cases, $\mathcal{E}_1$ overestimates the error while $\mathcal{E}_2$ and $\mathcal{E}_3$ underestimate it; however, all of the estimators yield effectivity and robustness indices (for the $\mathcal{E}_2$ and $\mathcal{E}_3$) close to one. The explanation given in Sect. 5.3 can also be used here to explain the influence of the *special*-enrichement on the error estimators. The $\mathcal{E}_4$ estimator exhibits reasonable performance, but poor values are again obtained by its lower bound version.

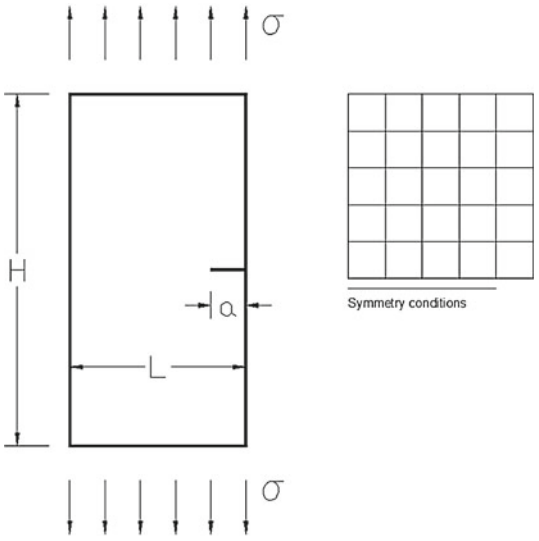

(a) Problem description **(b)** Discretization

Fig. 13 Problem description and discretization—$\sigma = 1.0$, $a = 2.0$, $L = 10.0$, $H = 20.0$, Young's modulus $E = 1.0$, Poisson ratio $\nu = 0.3$, thickness $t = 0.1$

Table 8 Global effectivity indices—p-refinement and no *special*-enrichment

p	$\mathcal{E}_1$	$\mathcal{E}_2$	$\mathcal{E}_2^I$	$\mathcal{E}_3$	$\mathcal{E}_3^I$	$\mathcal{E}_4$	$\mathcal{E}_4^I$	η (%)
1	1.224	0.852	0.687	0.873	0.641	0.755	0.320	19.52
2	1.273	0.679	0.672	0.690	0.600	0.608	0.410	14.43
3	1.352	0.664	0.651	0.712	0.592	0.631	0.516	13.46
4	1.379	0.611	0.630	0.716	0.544	0.592	0.431	11.45

Table 9 Global effectivity indices—p-refinement and *special*-enrichment

p	$\mathcal{E}_1$	$\mathcal{E}_2$	$\mathcal{E}_2^I$	$\mathcal{E}_3$	$\mathcal{E}_3^I$	$\mathcal{E}_4$	$\mathcal{E}_4^I$	η (%)
1	1.053	0.940	0.410	1.013	0.771	0.995	0.538	11.41
2	1.007	0.907	0.434	1.108	0.811	1.137	0.388	3.35
3	1.021	0.724	0.728	0.799	0.623	0.647	0.433	2.06
4	1.158	0.781	0.808	0.917	0.718	0.873	0.702	1.33

6 Final considerations

In this work, three versions of the subdomain-based residual method for a posteriori error estimators were investigated for the first time in the framework of the GFEM and for two-dimensional elasticity problems with smooth and non-smooth behavior. The non-smooth problems are described using both polynomial and non-polynomial functions to evaluate the error estimators. These estimators ($\mathcal{E}_2$, $\mathcal{E}_3$ and $\mathcal{E}_4$) were compared to an estimator based on an element residual approach, referred to as $\mathcal{E}_1$. The methods differ in the construction of the bi-linear form of the local error problem. The second and the third methods are based on [39,43,48]. The estimator $\mathcal{E}_4$ is first proposed in this paper and uses the product of the PoU functions and test functions as weights in the integral equation describing the error problem. The local problems obtained with these three subdomain-error techniques do not require the computation of traction jumps at element interfaces for the calculation of the residual data. Another advantage of the subdomain techniques is the direct determination of the error indicators associated with each node, which fits very well into the GFEM p-adaptive strategy.

Four numerical problems were presented, and the effectivity and robustness indices were evaluated. Two of these problems have smooth solutions and the other two have different levels of non-smooth solutions. These two types of problems were specifically chosen to identify how the degree of smoothness of the solution can affect the estimator behavior. In addition, *special* functions chosen to reproduce the singularity of the solution derivatives were used to enrich the GFEM approximation, and the impact of this technique on the estimators was also evaluated.

Based on the results obtained from the problems with non-smooth solutions, the presence of a singularity on the derivative field penalizes all four error estimators. The worst performance was observed for estimator $\mathcal{E}_4$. The inclusion of *special* functions that are capable of reproducing the singular character of the solution in the enrichment strategy significantly improves the quality of all four estimators evaluated in this paper. This improvement was observed when h- and p-refinements were performed with and without the *special* functions. In one of the examples, geometric enrichments are performed on an L-shaped plate (always keeping at least one element covered by patches enriched with the *special* functions). The local error distributions were also evaluated, and it was shown that the inclusion of the *special* functions not only provides a better solution but also minimizes the portion of the error that the residual method, based on a polynomial space, cannot estimate. In the last example, a plate with a crack, only the patch associated with the crack tip is enriched by the *special* functions, and p-enrichment is performed over the entire domain. In this strategy, the elements that share the node with the crack tip are enriched with a blend of polynomial and non-polynomial functions (the *special* functions). The approximation functions constructed over these elements form a basis for a space that is larger than that of the polynomial functions; however, it cannot exactly reproduce the *special* functions used to multiply the PoU. Nevertheless, good results for the error estimators were achieved, especially for the third type of error estimator ($\mathcal{E}_3$).

In some examples, the estimator $\mathcal{E}_4$ fails to produce a good lower estimate to the approximate error. In addition, note that the non-symmetric form of the problem resulting from Eq. (62) can negatively impact the code implementation. The

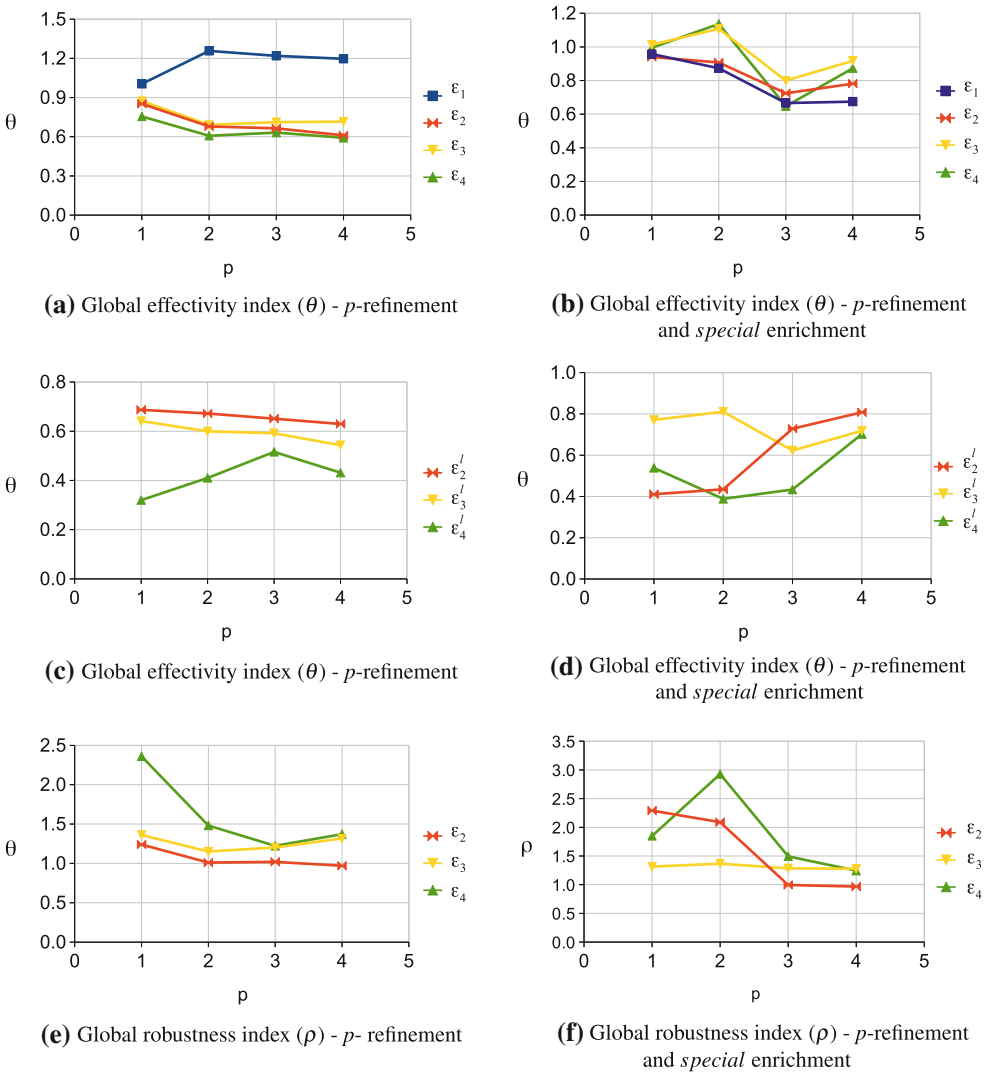

(a) Global effectivity index (θ) - p-refinement

(b) Global effectivity index (θ) - p-refinement and *special* enrichment

(c) Global effectivity index (θ) - p-refinement

(d) Global effectivity index (θ) - p-refinement and *special* enrichment

(e) Global robustness index (ρ) - p- refinement

(f) Global robustness index (ρ) - p-refinement and *special* enrichment

Fig. 14 Global effectivity (θ) and robustness (ρ) indices

different approach of this estimator indicates the need for an alternative formulation of the lower estimator given by Eqs. (54) and (55). Note that the sum of (55) may be underestimated by the cancellation of some terms. Further mathematical research should to be performed about this issue. Finally, the error indicators obtained from this approach have a different interpretation from the other two error estimates. The PoU functions are introduced in (57) not only to decompose the error problems into subdomains, but also to change the description of the error function. In this new description, the portion of the error approximation that arises from the node and its neighborhood plays a more important role than those arising from the element domain.

Regardless of the version of the subdomain error estimator ($\mathcal{E}_2$, $\mathcal{E}_3$ or $\mathcal{E}_4$), its extension to 3D problems appears to be not difficult. In the 3D case, the patch of elements is a solid formed by those elements sharing the same node. As in the 2D case, the PoU function is zero on the surface boundary (for internal patches), which means that there is no need to compute tractions along the element boundaries. The number of elements in each 3-dimensional patch is much higher than that for the 2-dimensional analysis. The size of the local problem therefore depends substantially on the type of mesh used. In 3D problems, a complex implementation of the equilibrium strategies demanded by $\mathcal{E}_1$ can lead to prohibitive computational costs. The flux-free characteristic of the subdomain error estimators avoids this handicap, which strongly offsets the burden arising from an increase in the size of the local problems, as observed by [30] when the subdomain strategy is discussed for the 3D analysis with the FEM. Care should be taken when the solution presents singular stress fields. In the case of cracks, for example, their complex geometry may not be planar, and an adequate analytical function therefore may not be

available to enrich the PoU. The standard Gauss quadrature may also fail. These are key issues of several studies on the GFEM/XFEM [19,25,26,29,34,41,49], which may have an important impact on the conclusions drawn in this paper regarding the subdomain error strategies. Additionally, comparisons with explicit approaches of error estimators, as those presented by [22] deserve to be pursued as a topic for further research.

Acknowledgments The first and second authors gratefully acknowledge the support of the Brazilian research agencies CNPq (in Portuguese—Conselho Nacional de Desenvolvimento Científico e Tecnológico—Grants 305626/2010-8 and 303315/2009-1), FAPEMIG (in Portuguese "Fundação de Amparo à Pesquisa do Estado de Minas Gerais"—Grant PPM-00244-11) and the Capes Foundation (Grant BEX9278/11-7). The third author gratefully acknowledges the support of U.S. Air Force office of Scientific Research under contract number FA9550-12-1-0379.

References

1. Ainsworth M, Oden JT (1997) A posteriori error estimation in finite element analysis. Comput Methods Appl Mech Eng 142:1–88
2. Babuška I, Melenk JM (1997) The partition of unity method. Int J Numer Methods Eng 40:727–758
3. Babuška I, Strouboulis T (2001) The finite element method and its reliability. Clarendon Press, Oxford
4. Babuška I, Caloz G, Osborn JE (1994) Special finite element method for a class of second order elliptic problems whith rough coefficients. SIAM J Numer Anal 31(4):745–981
5. Bank RE, Weiser A (1985) Some a posteriori error estimators for elliptic partial defferential equations. Math Comput 44:283–301
6. Barros FB, Proença SPB, de Barcellos CS (2004a) Generalized finite element method in structural nonlinear analysis—a p-adaptive strategy. Comput Mech 33(2):95–107
7. Barros FB, Proença SPB, de Barcellos CS (2004b) On error estimator and p-adaptivity in the generalized finite element method. Int J Numer Methods Eng 60(14):2373–2398
8. Barros FB, de Barcellos CS, Duarte CA (2007) p-Adaptive Ck generalized finite element method for arbitrary polygonal clouds. Comput Mech 41:175–187
9. Belytschko T, Black T (1999) Elastic crack growth in finite elements with minimal remeshing. Int J Numer Methods Eng 45:601–620
10. Belytschko T, Gracie R, Ventura G (2009) A review of extended/generalized finite element methods for material modeling. Model Simul Mater Sci Eng 17:043001
11. Bordas S, Duflot M (2007) Derivative recovery and a posteriori error estimate for extended finite elements. Comput Methods Appl Mech Eng 196:3381–3399
12. Bordas S, Duflot M, Le P (2007) A simple error estimator for extended finite elements. Commun Numer Methods Eng 24:961–971
13. CIMNE (2011) GID 10.0.5. http://gid.cimne.upc.es. Accessed 2 April 2011
14. Demkowicz L, Oden JT, Strouboulis T (1984) Adaptive finite elements for flow problems with moving boundaries. Part 1: variational principles and a posteriori error estimates. Comput Methods Appl Mech Eng 46:217–251
15. Díez P, Parés N, Huerta A (2004) Accurate upper and lower error bounds by solving flux-free local problems in śtars. Revue européenne des éléments finis 13:497–507
16. Duarte CA, Oden JT (1995) Hp clouds—A meshless method to solve boundary-value problem. Technical Report, TICAM, The University of Texas at Austin
17. Duarte CA, Oden JT (1996a) An h–p adaptive method using cloud. Comput Methods Appl Mech Eng 139:237–262
18. Duarte CA, Oden JT (1996b) Hp clouds—an hp meshless method. Numer Methods Partial Differ Equ 12:673–705
19. Duarte CA, Babuška I, Oden J (2000) Generalized finite element methods for three-dimensional structural mechanics problems. Comput Struct 77:215–232
20. Duflot M, Bordas S (2008) A posteriori error estimation for extended finite elements by an extended global recovery. Int J Numer Methods Eng 76:1123–1138
21. Fries TP, Belytschko T (2010) The extended/generalized finite element method: an overview of the method and its applications. Int J Numer Methods Eng 84(3):253–304
22. Gerasimov T, Rüter M, Stein E (2012) An explicit residual-type error estimator for q_1 quadrilateral extended finite element method in two-dimensinoal linear elastic fracture mechanics. Int J Numer Methods Eng 90:1118–1155
23. González-Estrada OA, Ródenas JJ, Bordas SPA, Duflot M, Kerfriden P, Giner E (2012) On the role of enrichment and statical admissibility of recovered fields in a-posteriori error estimation for enriched finite element methods. Eng Comput Int J Comput Aided Eng Softw 29(8):814–841
24. Gordon WJ, Hall CA (1973) Construction of curvilinear coordinate systems and applications to mesh generation. Int J Numer Methods Eng 7:461–477
25. Gravouil A, Moës N, Belytschko T (2002) Non-planar 3d crack growth by the extended finite element and level sets—Part ii: level set update. Int J Numer Methods Eng 53(11):2569–2586. doi:10.1002/nme.430
26. Kim DJ, Pereira JP, Duarte CA (2010) Analysis of three-dimensional fracture mechanics problems: a two-scale approach using coarse-generalized FEM meshes. Int J Numer Methods Eng 81(3):335–365. doi:10.1002/nme.2690
27. Ladevèze P, Maunder EAW (1996) A general method for recovering equilibrating element tractions. Comput Methods Appl Mech Eng 137:111–151
28. Lee NS, Bathe KJ (1993) Effects of element distortions on the performance of isoparametric elements. Int J Numer Methods Eng 36:3553–3576
29. Loehnert S, Mueller-Hoeppe DS, Wriggers P (2011) 3d corrected xfem approach and extension to finite deformation theory. Int J Numer Methods Eng 86(4–5):431–452. doi:10.1002/nme.3045
30. Mariné NP (2005) Error assessment for functional outputs of PDE's: bounds and goal-oriented adaptivity. Ph.D. Dissertation, Universidad Politécnica de Cataluña
31. Melenk JM (1995) On generalized finite element methods. Ph.D. Dissertation, University of Maryland, College Park
32. Melenk JM, Babuška I (1996) The partition of unity finite element method: basic theory and applications. Comput Methods Appl Mech Eng 39:289–314
33. Möes N, Dolbow J, Belytschko T (1999) A finite element method for crack growth without remeshing. Int J Numer Methods Eng 46:131–150
34. Moës N, Gravouil A, Belytschko T (2002) Non-planar 3d crack growth by the extended finite element and level sets—Part i: mechanical model. Int J Numer Methods Eng 53(11):2549–2568. doi:10.1002/nme.429
35. Oden JT, Duarte CA (1997) Clouds, cracks and FEM's. In: Reddy BD (ed) Recent developments in computational and applied

mechanics. International Center for Numerical Methods in Engineering, CIMNE, Barcelona, pp 302–321
36. Oden JT, Reddy JN (1976) An introduction to the mathematical theory of finite elements. Pure and applied mathematics. Wiley, New York
37. Oden JT, Demkowicz L, Rachowicz W, Westermann TA (1989) Toward a universal h–p adaptive finite element strategy, Part 2. A posteriori error estimation. Comput Methods Appl Mech Eng 77:113–180
38. Oden JT, Duarte CA, Zienkiewicz OC (1998) A new cloud-based hp finite element method. Comput Methods Appl Mech Eng 153:117–126
39. Parés N, Díez P, Huerta A (2006) Subdomain-based flux-free a posteriori error estimator. Comput Methods Appl Mech Eng 195:297–323
40. Park K, Pereira JP, Duarte CA, Paulino GH (2009) Integration of singular enrichment functions in the generalized/extended finite element method for three-dimensional problems. Int J Numer Methods Eng 78(10):1220–1257. doi:10.1002/nme.2530
41. Pereira J, Duarte C, Jiao X (2010) Three-dimensional crack growth with hp-generalized finite element and face offsetting methods. Comput Mech 46:431–453. doi:10.1007/s00466-010-0491-3
42. Prange C, Loehnert S, Wriggers P (2012) Error estimation for crack simulations using the XFEM. Int J Numer Methods Eng 91(13):1459–1474. doi:10.1002/nme.4331
43. Prudhomme S, Nobile F, Chamoin L, Oden JT (2004) Analysis of a subdomain-based error estimator for finite element approximations of elliptic problems. Numer Methods Partial Differ Equ 20(2):165–192
44. Ródenas JJ, González-Estrada OA, Tarancón JE, Fuenmayor FJ (2008) A recovery-type error estimator for the extended finite element method based on singular + smooth stress field splitting. Int J Numer Methods Eng 76:545–571
45. Stein E, Gerasimov T, Rüter M (2011) Explicit and implicit residual-type goal-oriented error estimators for xfem in lefm. In: Díez P Aubry DV (eds) International Conference on Adaptive Modeling and Simulation, ADMOS
46. Strouboulis T, Babuška I, Copps K (2000) The design and analysis of the generalized finite element method. Comput Methods Appl Mech Eng 181(1–3):43–69
47. Strouboulis T, Copps K, Babuška I (2001) The generalized finite element method. Comput Methods Appl Mech Eng 190:4081–4193
48. Strouboulis T, Zhang L, Wang D, Babuška I (2006) A posteriori error estimation for generalized finite element methods. Comput Methods Appl Mech Eng 195:852–879
49. Sukumar N, Chopp DL, Moran B (2003) Extended finite element method and fast marching method for three-dimensional fatigue crack propagation. Eng Fract Mech 70:29–48
50. Szabó B, Babuška I (1991) Finite element analysis. Wiley, New York
51. Timoshenko SP, Goodier JN (1970) Theory of elasticity. McGraw-Hill Book Co., Inc., New York
52. Xiao QZ, Karihaloo BL (2006) Improving the accuracy of xfem crack tip fields using higher order quadrature and statically admissible stress recovery. Int J Numer Methods Eng 66:1378–1410
53. Zienkiewicz OC, Zhu Z (1987) A simple error estimator and adaptive procedure for practical engineering analysis. Int J Numer Methods Eng 24:337–357